

Coronal Mass Ejections: Masses, Dynamics and Shock Kinematics

A dissertation submitted to the University of Dublin
for the degree of *Philosophiae Doctor (PhD)*

Eoin P. Carley
Trinity College Dublin, December 2013

SCHOOL OF PHYSICS
UNIVERSITY OF DUBLIN
TRINITY COLLEGE



Declaration

I declare that this thesis has not been submitted as an exercise for a degree at this or any other university and it is entirely my own work.

I agree to deposit this thesis in the University's open access institutional repository or allow the library to do so on my behalf, subject to Irish Copyright Legislation and Trinity College Library conditions of use and acknowledgement.

Name: Eoin Carley

Signature: **Date:**

Summary

Coronal mass ejections (CMEs) are large-scale eruptions of magnetized plasma from the low solar atmosphere into interplanetary space. With energies of up to 10^{26} J, they are the most energetic eruptive phenomena in the solar system and are also the driver of plasma shocks from the corona into the heliosphere. Despite many years of study, the nature of the forces governing their eruption, and the kinematical behavior of the resulting shock, remain poorly understood. This thesis will presents the first accurate calculation of the magnitude of the total force on a CME. I will also show a previously unseen plasma shock behavior that sheds new light into the kinematical nature of CME-driven shocks in the corona.

In the past, measurement of the forces governing the propagation of CMEs have been hindered by highly uncertain estimates of the total mass of the ejection. The primary source of uncertainty is the unknown position and geometry of the CME, leading to an erroneous treatment of the Thomson scattering equations which are used to estimate the mass. Geometrical uncertainty on the CMEs position and size has primarily been due to observations of the eruption from a single vantage point. However, with the launch of the STEREO spacecraft, the two viewpoints can be exploited to derive the CMEs position and size, ultimately resulting in mass uncertainty that is both reliably quantified and much reduced. These much better estimates for the mass can then be combined with kinematical results that are also more reliable and hence lead to the first reliable quantification of the total force acting on the CME.

This thesis will present the method by which mass values derived from the STEREO coronagraphs, and the uncertainties reliably quantified. Combining this with a previous kinematical analysis, the mechanical energies and total force on the CME is derived. Using the magnetohydrodynamical equation of motion, the relative sizes of the forces at each stage in the CME propagation are estimated, revealing the Lorentz force is the largest source of CME acceleration early in its propagation. This analysis also leads to a reliable observational estimate of size of this Lorentz force.

CMEs often erupt at speeds in excess of the local MHD wave speeds in the corona. Traveling in excess of Mach 1, they often drive shocks which can have a variety of manifestations, from radio bursts to the propagation of bright pulse seen in extreme ultraviolet (EUV) images. Despite these myriad shock phenomena being observed for decades, the relationship between them remains unknown. Chapters X and Y of this thesis, will describe the construction of instrumentation to observe high time sampling spectroscopy of these radio bursts. These observations are combined with high cadence radio and EUV images to reveal the presence of a shock driven by the expansion of the CME flank that resulted in both the EUV pulse and radio burst. Furthermore, the radio spectra evidence for particle acceleration at this shock is presented, revealing the shock was capable of producing a bursty acceleration of near-relativistic electrons. This previously unseen behavior sheds new light on the physics governing radio burst generation and the relationship to CMEs and EUV pulses.

For my parents.

Acknowledgements

Some sincere acknowledgements...

List of Publications

1. **Carley, E. P.**, MacAteer, R. T. J., & Gallagher, P. T.
“Coronal Mass Ejection Masses, Energies, and Force Estimates Using *STEREO*”,
The Astrophysical Journal, Volume 752, Issue 1, article id. 36, 8 pp. (2012).
2. Zucca, P., **Carley, E. P.**, McCauley, J., Gallagher, P. T. ,Monstein, C., &
MacAteer, R. T. J.,
“Observations of Low Frequency Solar Radio Bursts from the Rosse Solar-Terrestrial Observatory”,
Solar Physics, Volume 280, Issue 2, pp.591-602. (2012).
3. **Carley, E. P.**, Long, D. M., & Gallagher, P. T.
“Shock Acceleration of Energetic Particles in the Solar Atmosphere”,
Some Journal, Volume X, Issue Y, article id. (2013)
4. Zucca, P., **Carley, E. P.**, Bloomfield, S. D., & Gallagher, P. T.
“Density and Alfvén....”,
Some Journal, Volume X, Issue Y, article id. (2013)
5. Bloomfield, S. D., **Carley, E. P.**,
“A Comprehensive Overview of the 2011 June 7 Solar Storm”,
Astronomy & Astrophysics, Volume X, Issue Y, article id. (2013)

Contents

List of Publications	vii
List of Figures	xi
List of Tables	xvi
1 Introduction	1
1.1 The Sun	2
1.1.1 Solar Interior	2
1.1.2 Solar Magnetic Field and Dynamo	8
1.1.3 Solar Atmosphere	11
1.1.3.1 Photosphere	11
1.1.3.2 Chromosphere	13
1.1.3.3 Corona	15
1.2 Coronal Mass Ejections and Coronal Shocks	18
1.2.1 CMEs	18
1.2.2 CMEs and Shocks	18
1.2.3 Open Questions	18
2 Coronal Mass Ejection and Plasma Shock Theory	19
2.1 Plasma Physics and Magnetohydrodynamics	19
2.1.1 Maxwell's Equations	19
2.1.2 Plasma Physics and Boltzmann Equation	20
2.1.3 Magnetohydrodynamics	20
2.1.4 Magnetic Reconnection	20
2.1.5 MHD Shocks	20
2.2 Coronal Mass Ejections	27

CONTENTS

2.2.1	Catastrophe Model	27
2.2.2	Magnetic Breakout Model	27
2.2.3	Toroidal Instability	29
2.2.4	Drag Models	32
2.3	Coronal Shocks and Plasma Emission	32
2.3.1	Shock Particle Acceleration	32
2.3.2	Wave-Particle Interaction	32
2.3.3	Three-Wave Interaction and Plasma Emission	32
3	Observation and Instrumentation	35
3.1	Thompson Scattering Theory	35
3.1.1	Thomson Scattering in the Corona	35
3.1.2	White-light observations of CMEs	38
3.2	Coronagraphs	38
3.2.1	Lyot Coronagraph	38
3.2.2	STEREO COR1 and COR2	38
3.2.3	SOHO LASCO	40
3.3	Radio Spectrometers and Radioheliographs	40
3.3.1	RSTO Callisto	40
3.3.2	STEREO WAVES	40
3.3.3	Nancay Decametric Array	40
3.3.4	Nancay Radioheliograph	40
3.4	EUV imaging	40
3.4.1	SDO AIA	40
4	Coronal Mass Ejection Masses, Energetics, and Dynamics	43
4.1	Masses	43
4.1.1	Observations	45
4.1.2	Evaluation of Uncertainties	48
4.1.3	Masses	52
4.2	Energies and Dynamics	55
4.2.1	Forces acting on CMEs	58
4.3	Conclusion	60

CONTENTS

5 Coronal Mass Ejection Masses, Shocks, and Particle Acceleration	62
5.1 Radio Bursts	62
5.1.1 Type II, Type III, and Herringbones	62
5.2 EUV Wave and Radio Source	62
5.2.1 Relationship with Radio Spectra	62
5.3 Role of the CME	62
5.3.1 CME Bow Shock	62
5.3.2 Relationship Between CME, CBF, and Radio bursts	62
A A Nice Appendix	63
References	64

List of Figures

1.1	The internal structure of the Sun, including the core, radiative zone, and convective zone. Also shown is the structure of its atmosphere, including the photosphere, chromosphere, and corona. The layers of the solar atmosphere are usually demarcated by temperature changes as height above the solar surface increases. The temperature ranges from \sim 6000 K in the photosphere to above 1 MK in the corona.	6
1.2	Helioseismological determination of interior rotation rate in nanoHertz (nHz) as a function solar radius, starting from solar centre ($r = 0.0$) to surface ($r = 1.0$). The separate symbols show different latitudes, from 0° to 75° . The data show that the interior rotates differentially down to $\sim 0.7 R_\odot$. The dashed line demarcates the boundary between solid body rotation and differential rotation (Thompson <i>et al.</i> , 2003).	7
1.3	Top: The latitude of sunspots as a function of time. During the rise phase of each cycle the sunspots have a latitudinal distribution of $\pm 30^\circ$ from the equator. As the solar cycle progresses, sunspots emergence takes place at an increasingly lower latitude. Bottom: Sunspot area as a function of time. The approximate 11 year periodicity is clearly shown.	9

LIST OF FIGURES

1.4	Differential rotation and flux freezing result in the poloidal dipolar magnetic field, generated by dynamo action, to be dragged around in a toroidal direction, an action known as the omega effect. Buoyancy of the field lines results in them rising and twisting, known as the alpha effect, eventually surfacing to become bipolar fields that extend far into the corona.	10
1.5	Temperature and density variation in the solar atmosphere constructed from the models of (Fontenla <i>et al.</i> , 1988; Gabriel, 1976; Vernazza <i>et al.</i> , 1981), adopted from (Phillips <i>et al.</i> , 2008).	14
1.6	Atmospheric Imaging Assembly 171 Å image of the solar corona. Bright regions are strong concentrations of magnetic fields known as active regions (temperatures of 2 – 6 MK). Areas outside these regions are known as quiet sun (temperatures 1 – 2 MK).	16
2.1	Orientation of magnetic field and velocity field with respect to shock plane, in the rest frame of the shock. Shock normal in this case would be along the $-x$ direction i.e., into upstream region 1. (Fitzpatrick, 2000)	21
2.2	Predicted band splitting ratio δ_{bs} as a function of Mach number and magnetic field orientation with respect to shock normal. Flow is anti-parallel to shock normal (head-on). Both image and surface are shown, left and right respectively. On the left, the red contours show specific values of of band-splitting. Note that for small mach numbers the level of band splitting is independent of magnetic field orientation. It is only at Mach numbers greater than ~ 2.1 that the B-field orientation becomes important.	26

LIST OF FIGURES

2.3	The breakout model, consisting of a quadrupolar flux system in which the central flux (blue) is flanked by to side lobe flux systems (green), with the entire system kept in stability by the tension of the overlying red field. Shearing and/or twisting on the underlying flux causes it to grow slowly. Eventually a current sheet forms at the magnetic null above the central flux, causing reconnection. This reconnection transfers overlying field to the side-lobes, effectively creating a conduit for the central flux to escape as a CME (Lynch <i>et al.</i> , 2008).	28
2.4	The flux rope model of Chen (1989), used to study the toroidal instability of a twisted flux system in the corona.	31
3.1	The white-light corona during a solar eclipse. Occultation of the bright solar disk by the moon reveals the faint outer atmosphere of the Sun, known as the corona. It is highly structured, showing features like streamers and plumes. <i>Eclipse photograph courtesy of Miloslav Druckmüller</i> http://www.zam.fme.vutbr.cz	36
3.2	Geometry of single electron scattering in the solar atmosphere, with angles Ω and χ	37
3.3	A schematic of the basic optical design of the Lyot coronagraph. Lyot's key inventions where the placement of a Lyot stop and Lyot spot at the positions where diffracted light would contaminate the image and obscure the faint corona.	39
3.4	A schematic of the basic optical design of the COR1 coronagraph. There are two such identical instruments, one on the Ahead and one on the Behind spacecraft. It is the same basic design as the Lyot coronagraph with the addition of baffles to prevent scattered light and a polarizer behind the Lyot stop (Thompson & Reginald, 2008).	41

LIST OF FIGURES

3.5 A schematic of the basic optical design of the COR2 coronagraph. This is an externally occulted coronagraph, meaning it has an extra occultation disk in front of the objective lens. This results in less internally scattered light, but also results in an obscuration of the inner corona. As with COR1, there are two such identical instruments, one on the Ahead and one on the Behind spacecraft (Howard <i>et al.</i> , 2008)	42
4.1 Selection of base difference images of the CME in COR1 A (top row) and COR1 B (bottom row), with pixel values of grams. The CME is quite faint in the A images and appears not to have as much structure as in B. There is a large contribution to mass from a near-saturated region to the upper flank of the CME in the B images. Such saturation in the mass images coincides spatially with the prominence in total brightness images.	46
4.2 Selection of base difference images of the CME in COR2 A (top row) and COR2 B (bottom row), with pixel values of grams. The CME is clearly distinguishable in both fields of view. Only the B field view shows clearly the three part structure of core, cavity and front. The COR2 B images were used to measure core and front mass separately	47
4.3 Schematic showing the relative orientation of the line-of-sight (LOS), and the plane-of-sky (POS). Electron position is at point P and C is Sun center. The vector CP may also represent CME propagation direction. Scattering efficiency is heavily dependent on the angle θ (or χ) and is least efficient when $\theta = 0^\circ$ ($\chi = 90^\circ$).	49

LIST OF FIGURES

- 4.4 CME mass development with height (a) and time (b), for the 2008 December 12 CME. After \sim 08:00 UT ($\gtrsim 5 R_{\odot}$) the masses from the inner and outer coronagraphs are summed to show uninterrupted mass development from \sim 2–20 R_{\odot} over a period of 12 hours. The small bump in the CME mass at \sim 07:00 UT ($\sim 4 R_{\odot}$) is probably due to an unknown amount of H- α emission from the prominence. Mass of CME front and core are also shown, red ‘ \times ’ and blue square, for COR2B, panel (b). After 14:52 UT they share approximately equal mass. The inset of (a) shows mass development with height for COR2B only; the red curve represents a fit to the data whereby the mass asymptotically approaches $3.4 \pm 1.0 \times 10^{15}$ g.

4.5 (a) CME velocity as a function of heliocentric distance, including a fit to the data produced using an aerodynamic drag model beyond $\sim 7 R_{\odot}$ (Byrne *et al.*, 2010). (b) Acceleration of CME, including fit, derived from the velocity data and fit. Panel (c) and (d) show the kinetic energy and force, respectively, both calculated using constant CME mass of $3.4 \pm 1.0 \times 10^{15}$ g and kinematics results from (a) and (b). Also shown are the fits to energy and force produced from fits to velocity and acceleration.

53

56

List of Tables

1

Introduction

The Sun has long been the focus of humanity's curiosity. Throughout history it has been the harbinger of new religions, philosophies, and sciences. It has changed our understanding of our place in the Universe and allowed us to push forward the frontiers of stellar astronomy. Although our understanding of the Sun is nowadays more advanced, the curiosity we hold for it has not changed since the very early humans. Now, we understand the Sun is a star similar to any other in its class, currently going through a relatively unchanging 11 year cycle of activity that is extremely rich in physical complexity. The study of such complex phenomena has yielded immeasurable advances in many areas of physics such as spectroscopy, plasma physics, magnetohydrodynamics (MHD), particle physics, to name but a few. Although some of these sciences have grown over decades (or even centuries) they are still incomplete. I hope this theses, in some small way, will contribute to the continuing growth of these sciences and to the understanding of our nearest star.

1.1 The Sun

The Sun is our nearest star, located 1.49×10^6 km from Earth at the centre of our solar system. Located on the main sequence of the Hetzspring-Russel (HR) diagram, it has a spectral class of G2V, with a luminosity of $L_\odot = (3.84 \pm 0.04) \times 10^{26}$ W, mass of $M_\odot = (1.989 \pm 0.0003) \times 10^{30}$ kg and radius of $R_\odot = (6.959 \pm 0.007) \times 10^8$ m (Foukal, 2004). It was born approximately 4.6×10^9 years ago when a giant molecular cloud underwent gravitational collapse and began hydrogen nuclear fusion at its centre (reference). The energy produced from this fusion resulted in enough pressure to counteract gravitational contraction and bring about a hydrostatic equilibrium, allowing the young star to reach a stability that is sustained today. It is estimated the Sun will maintain this stability for another 5 billion years, at which point, it will move off the main sequence and into a red giant phase. During this later part of its life, it will grow in size to 100 times its current radius and begin nuclear burning of heavier elements such as carbon and oxygen. Once carbon burning in the core has ceased it can no longer sustain nuclear fusion of heavier elements, resulting in a gravitational instability that will eventually lead to a stellar nova. This nova will result in the loss of the outer envelopes and ultimately the Sun's death, leaving behind a compact and dense white-dwarf.

Until such time, the Sun will remain on the main sequence in a regular state of hydrogen fusion in its core. The energy released during this process is the ultimate source of light and all energetic activity that we observe from Earth and beyond. Before we can understand how this energy manifests in the solar atmosphere as a variety of energetic phenomena, it is important to understand how the energy is generated and transported through its interior and finally released into its atmosphere and interplanetary space.

1.1.1 Solar Interior

The theoretical development on how the solar interior is structured and how it behaves has been through what is known as the ‘standard solar model’ or SSM. The SSM is a grouping of theories that described how the Sun was formed, how it maintains its stability, how it generates energy, and how this energy is transported

through its interior and released at the surface. Much of the major developments of this theory have been in the 20th century, due mainly to the pioneering experiments in solar neutrino physics and helioseismology. Hence, the development of the SSM has mainly been through a refinement of the theory based on these observational fields. Although the SSM has increased in sophistication, its four main aspects remain the most general framework for describing the behavior of the solar interior.

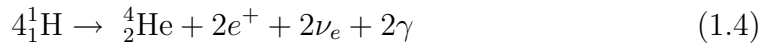
The SSM firstly states that the Sun was born from the gravitational collapse of a primordial gas of hydrogen, helium, and traces of other heavy elements. Secondly, it maintains its structural stability via a hydrostatic equilibrium such that the gravitational force is balanced by a pressure gradient ($\nabla P = -\rho g$) at each radial distance inside the star. The third main aspect of the SSM involves the source of the Sun's energy. Much of the early ideas proposed during the 19th century involved some form of chemical reaction or energy released during a slow gravitational contraction. However, during the first half of the 20th century the theory that the Sun is at least as old as the Earth began to come into focus. The idea of the Sun being more than 4.5 billion years old prompted the question of what energy source could sustain the Sun's luminosity for such a length of time. It was soon realised that thermonuclear fusion must be the source of such energy, and, as a result, it should be possible to observe the neutrino products of this fusion. Hence, starting in the 1950s a number of pioneering neutrino physics experiments were developed in an attempt to detect solar-generated neutrinos at Earth. These pioneering experiments, as well as there more sophisticated counterparts today, confirm much of the theories on solar core energy generation.

From the 1950s onwards there has been a confirmed detection of neutrinos generated in a hydrogen fusion process, namely the proton-proton or ‘pp’-chain, in the solar core. In this process, four protons are fused to form a helium nucleus. This can occur in a variety of ways, but at the Sun’s core temperature of 15 MK, the dominant reaction is the pp 1 chain given by





where ${}^1_1\text{H}$ is a hydrogen nucleus, ${}^2_1\text{H}$ is deuterium, ${}^3_2\text{He}$ is tritium, ${}^4_2\text{He}$ is helium, e^+ is a positron, ν_e is an electron neutrino, and γ is a gamma ray photon. Reactions (1.1) and (1.2) must happen twice for (1.3) to occur. Taking this into account, the entire process may be summarised as



liberating $4.2 \times 10^{-12}\text{J}$ of energy, with $\sim 2.4\%$ of the energy carried away by the neutrinos. This particular form of the pp-chain (pp 1) occurs in 86% of the cases (Turck-Chièze & Couvidat, 2011). However, there are other reactions capable of producing He from H categorized into pp II, pp III etc, which each involve production of ${}^7\text{Be}$ and ${}^8\text{B}$. The initial neutrino detections at Earth were the result of the pp III reaction which involves the creation of ${}^8_5\text{B}$, followed by a decay to ${}^8_4\text{Be}$, a positron, and an electron neutrino (Davis *et al.*, 1968). These early detections and the results of more recent experiments such as the SuperKamiokande (Fukuda *et al.*, 1998) show that the expected neutrino flux given by the standard solar model is smaller than the observed. This deficit in neutrino flux observations became the famed ‘solar neutrino problem’ during the 1970s. One of the proposed explanations for the process was via an oscillation of the neutrino amongst three sets of ‘flavors’ i.e., the neutrino can be either an electron ν_e , muon ν_μ , or tau ν_τ neutrino. With the original detectors only being able to detect the ν_e , this would result in a flux deficit (non-detection of ν_μ and ν_τ). This oscillation amongst three flavors was given the name the ‘MSW effect’ after Mikheev & Smirnov (1986) and Wolfenstein (1978), and later confirmed experimentally by the SuperKamionkande experiment.

The neutrino experiments together with the standard solar model SSM provide much of what we know about the solar energy generation and the solar core. They imply a temperature of $15.6 \times 10^6\text{K}$ and density of $1.48 \times 10^5\text{kg m}^{-3}$ at solar centre, and also confirm the existence of a variety of pp reactions (pp 1 to

pp IV), and some level of Carbon-Nitrogen-Oxygen (CNO) fusion process. These fusion processes occur over $0.0 - 0.25 R_{\odot}$ (Figure 1.1), which defines the solar core. Outside the core the temperature drops to a value such that fusion ceases. While thermonuclear fusion is the third aspect of the SSM involves the generation of solar energy, the fourth aspect involves exactly what happens to this energy once it is generated i.e., it describes an energy transport mechanism.

Beyond $0.25 R_{\odot}$ the temperature drops to 8 MK, such that fusion stops but only free protons and electrons exist. In this environment, the photons continuously scatter off free particles, undergoing a random walk toward the surface over a distance of $0.25 - 0.7 R_{\odot}$. This region is known as the radiative zone and has densities of $2 \times 10^4 - 2 \times 10^2 \text{ kg m}^{-3}$, resulting in a small photon mean free path (mfp) of $9.0 \times 10^{-4} \text{ m}$. The photons proceed towards the solar surface over a very long time scale, taking on the order of 10^5 years to traverse this region (Mitalas & Sills, 1992). If radiative energy transport occurs, it will result in the following temperature gradient

$$\frac{dT}{dr} = -\frac{3}{16\sigma} \frac{\kappa\rho}{T^3} F_{rad} \quad (1.5)$$

where σ is the Stefan-Boltzmann constant, κ is the mass extinction coefficient (opacity per unit mass), ρ is mass density, T is temperature, and F_{rad} is the outward radiative flux. This implies that for a particular outward flux, if the opacity increases, a steeper temperature gradient is required to maintain such a flux. At $0.7 R_{\odot}$ the temperature drops to 1 MK allowing protons to capture electrons into a bound orbit. The existence of electrons in atomic orbit results in a dramatic increase in opacity of the plasma (Turck-Chièze & Couvidat, 2011) and hence the temperature gradient increases. The increased temperature gradient required to sustain the energy flow may lead to the onset of a convective instability beyond $0.7 R_{\odot}$ toward the solar surface. This instability will occur if the temperature gradient in the star is steeper than the adiabatic temperature gradient

$$\left| \frac{dT}{dr} \right|_{star} > \left| \frac{dT}{dr} \right|_{adiabatic} \quad (1.6)$$

This is known as the Schwarzschild criterion, and it is fulfilled from $0.7 - 1 R_{\odot}$ – a region known as the convection zone. The temperature and density drop as

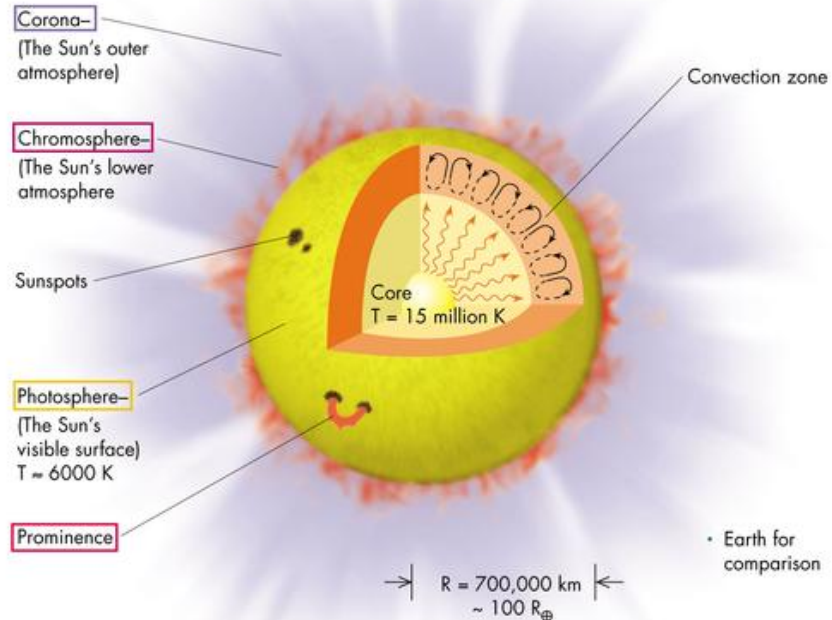


Figure 1.1: The internal structure of the Sun, including the core, radiative zone, and convective zone. Also shown is the structure of its atmosphere, including the photosphere, chromosphere, and corona. The layers of the solar atmosphere are usually demarcated by temperature changes as height above the solar surface increases. The temperature ranges from ~ 6000 K in the photosphere to above 1 MK in the corona.

height increases and finally reaches $T \sim 6000$ K and mass densities of $\rho \sim 1 \times 10^{-5} \text{ kg m}^{-3}$. Although no complete theoretical treatment of convection exists, mixing length theory and hydrodynamical modeling are used to determine how convection occurs in the solar interior. Convection ceases at $1 R_\odot$, where the environment makes a sudden transition to convectively stability. At this point the opacity drops and energy is released in the form of radiation, demarcating the start of the solar surface, known as the photosphere.

Much of what we know about the depth, temperature, and density of the convection zones come from a fine-tuning of the standard solar model, such that the model reproduces observations from neutrino and helioseismology experiments. In fact helioseismology alone can indicate great detail of the internal structure of

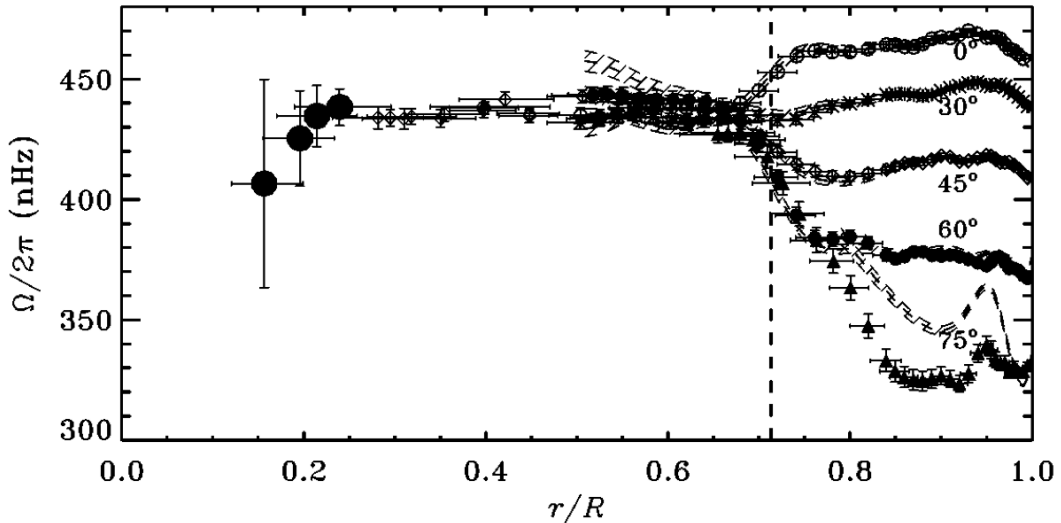


Figure 1.2: Helioseismological determination of interior rotation rate in nanoHertz (nHz) as a function solar radius ($r = 0.0$) to surface ($r = 1.0$). The separate symbols show different latitudes, from 0° to 75° . The data show that the interior rotates differentially down to $\sim 0.7 R_\odot$. The dashed line demarcates the boundary between solid body rotation and differential rotation (Thompson *et al.*, 2003).

the Sun. This field makes use of the fact the Sun acts as a resonator for acoustic waves which manifest as detectable oscillations in the doppler shift of photospheric Fraunhofer lines. These acoustic waves are referred to as pressure or p-modes, and a variety of wavelengths exist. Wavelengths that are an integer multiple of the solar cavity may exist as standing wave modes. Such wave modes have a period of approximately 5 minutes (Turck-Chièze & Couvidat, 2011).

The shorter wavelengths in the mode propagate into the solar convection zone and experience a total internal reflection at a shallow depth, while longer wavelengths can penetrate into much deeper layers. Hence depending on the period observed, the oscillations provide a probe of the internal thermodynamic properties at a particular level. Once such property closely monitored is the sound speed, which is seen to match the predicted sound speed based on the standard model. However, the observation and prediction show the biggest deviation at a depth of $0.3 R_\odot$, which is the region where the radiative zone transitions to the

convective zone. This obviously implies that SSM is lacking in its description of how the solar interior is stratified at this depth. This partly due to the fact the SSM does not take into account differential rotation. The solar surface rotates faster at the equator than it does at the poles i.e., angular velocity is stratified with latitude. Helioseismology has revealed that such differential rotational continues to the bottom of the convection zone. In the deeper radiative zone and core the Sun rotates as a solid body see Figure 1.2. There is a dramatic change in the internal dynamics when transitioning from convective to radiative zones.

As predicted by sound speed measurements and differential rotation, the region sandwiched in between radiative and convective zones is and extremely important boundary. It is known as the tachocline, and the dynamics of this thin layer is believed to play and extremely important role in the generation and evolution of the solar magnetic field (Thompson *et al.*, 2003).

1.1.2 Solar Magnetic Field and Dynamo

The solar magnetic field is the ultimately source of all energetic activity in the its atmosphere. At solar activity minimum the solar magnetic field has a poloidal dipolar structure, with the polar axes generally being coincident with the rotational axes. However as the the activity cycle progresses towards a maximum, the field gains a strong toroidal component, making it far more dynamic and complex. This complex toroidal component manifests at the surface as sunspots, hence the number of sunspots on disk has been used as a proxy for the activity cycle for over 100 years, often showing an approximate 11 year periodicity (Figure 1.3, bottom panel). At the beginning of the cycle sunspots tend to appear on disk with a latitudinal distribution of $\pm 30^\circ$ of the equator. As the cycle progresses, sunspots appear at lower and lower latitude (known as Spörer's law), until they eventually disappear at the end of a cycle. Sunspot latitude with respect to time is shown in Figure 1.3, top panel, and is known as the butterfly diagram.

Sunspots in there simplest case emerge as a dipole structure, with the leading spot being closer to the equator, such that the dipole is titled relative to the solar equator (Joy's law). In a given hemisphere, the leading sunspot and trailing spot have opposite polarities, with the polarities reversed in the other hemisphere

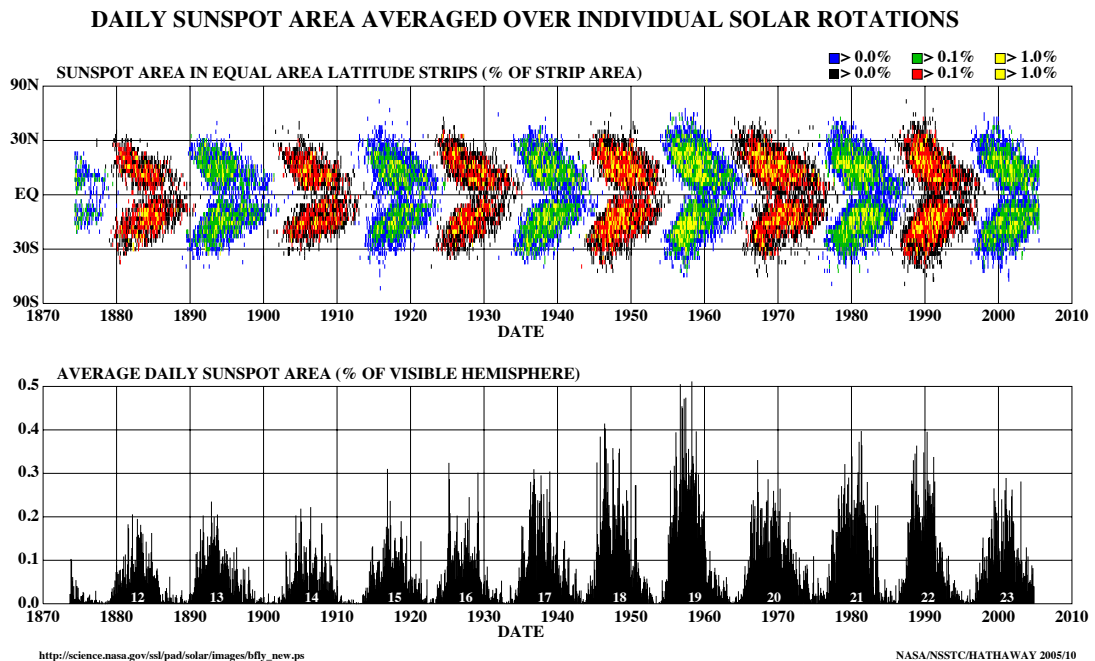


Figure 1.3: Top: The latitude of sunspots as a function of time. During the rise phase of each cycle the sunspots have a latitudinal distribution of $\pm 30^\circ$ from the equator. As the solar cycle progresses, sunspots emergence takes place at an increasingly lower latitude. Bottom: Sunspot area as a function of time. The approximate 11 year periodicity is clearly shown.

(Hayle's law). The trailing polarity can often be more fragmented and dispersed than the leading polarity. Despite sunspots generally having a dipolar structure, spot groups can be far more complex, having a multipolar structure (this will be described more later).

Over the course of a solar cycle, the sun changes polarity (at the time of sunspot maximum). For example, an overall dipolar configuration of North-South will become South-North, another cycle will bring it back to N-S once more. While the activity cycle usually last 11 years, one full magnetic cycle has a period of 22 years.

The complex behavior of the solar magnetic field over an 11 year activity cycle, during which the dipole flips, is generally explained by solar dynamo the-

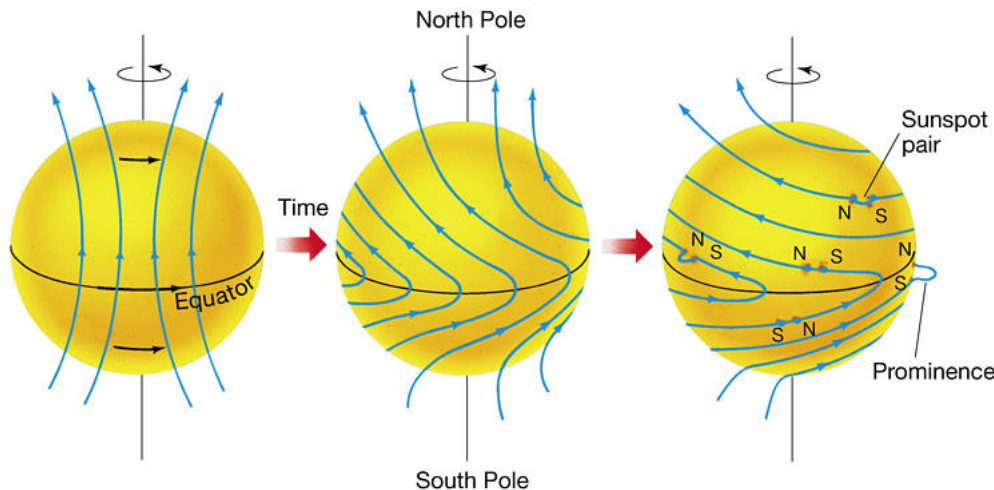


Figure 1.4: Differential rotation and flux freezing result in the poloidal dipolar magnetic field, generated by dynamo action, to be dragged around in a toroidal direction, an action known as the omega effect. Buoyancy of the field lines results in them rising and twisting, known as the alpha effect, eventually surfacing to become bipolar fields that extend far into the corona.

ory. This involves large-scale flow patterns of the solar interior that act to both induct and diffuse the magnetic field such that it produces the familiar 11 year magnetic activity cycle. Magnetohydrodynamics (MHD) is employed such that the magnetic induction equation and velocity field equation (equation of motion) are solved in numerical models to produce a toroidal field from a poloidal one, a process known as the Ω -effect. The theories must adhere to the constraints provided by observations of the sunspot cycle (Spörer's, Joy's, and Hale's laws), and also helioseismology observations of how the interior is structured.

Babcock (1961) first proposed a mechanism whereby the differential rotation of the solar convection zone tends to drag the field from a poloidal position into a toroidal one, eventually winding the field into a stressed state, see Figure 1.4. The main storage of this wound field is in the region below the convection zone known as the tachocline. This region is known as an 'overshoot' layer, in which descending convective flows are trapped due the subadiabicity of the region (convectively stable). This stability allows field to be built up and stored into complex magnetic structures. Parts of this structure may form a twisted mag-

netic 'flux-rope', and due to it's excess magnetic pressure, it becomes convectively unstable and begins to rise. During this rise a Coriolis force has a tendency to tilt into a north-south orientation and eventually penetrate through the solar surface and into the atmosphere, known as the α -effect (the tilt from Coriolis effects explains Joy's law). Dynamo theory attempts to explain the Ω -effect wrapping and build up of toroidal flux in the solar interior via inductive plasma flows (Charbonneau, 2010), particularly using the observed flow structure from helioseismology. Further MHD of convective instabilities is employed to describe the α -effect rise of flux systems into the solar atmosphere from the stably convective tachocline/overshoot layer. This is very much a study in itself, and describes the eventual formation coronal active regions from sub-photospheric flux-systems (Fan, 2009).

1.1.3 Solar Atmosphere

The solar atmosphere begins above the visible surface of the sun, known as the photosphere. At this point, the Sun become optically thin to visible radiation and light escapes from this surface. Beyond this visible surface is the solar chromosphere, the corona, which eventually becomes the solar wind. Each of these layers is home to a complex array of phenomena, and each layer with it's accompanying attributes is described here.

1.1.3.1 Photosphere

As mentioned the photosphere begins where the atmosphere become optically thin. 'Visible light' in this instance is usually taken to mean light with a wavelength of 5000 Å, hence the emergent light from the photosphere is taken to come from the surface at which $\tau_{5000} = 2/3$. This is a consequence of the Eddington-Barbier approximation, and says that emergent flux F_ν from the photosphere is given by

$$F_\nu = \pi B_\nu (\tau = 2/3) \quad (1.7)$$

e.g., the emergent flux is given by π times blackbody intensity at an optical depth of $2/3$, where blackbody intensity B_ν is given by Planck's law

$$B_\nu = \frac{2h\pi\nu^3}{c^2} \frac{1}{\exp(h\nu/k_B T) - 1} \quad (1.8)$$

where h is Planck's constant, ν is frequency, c is the speed of light, k_B is Boltzmann's constant, and T is temperature. Integrated over frequency this results in $F = \sigma T^4 (\tau = 2/3)$, where the frequency integrated flux is proportional to the temperature at $\tau = 2/3$, hence the effective temperature of solar blackbody radiation is $T_{eff} = T(\tau = 2/3) = 5800$ K. Solar radiation at visible wavelengths is most closely characterised by a blackbody of temperature 5800 K, although the brightness temperature T_B the solar photosphere can deviate from this value, since not all frequencies emerge from the same optical depth.

The visible appearance of the photosphere reveals a small scale granular structure, with granules of typical size scale of 1000 km with a lifetime of 5-10 minutes. The granules typically show bright centers surrounded by darker intergranular lanes. Doppler measurements reveal that granule centres have a positive (upward) velocity of up to $\sim 1 \text{ km s}^{-1}$, with intergranular lanes having a negative (downward) velocity. Such upward and downward flow reveals that granulation at the photosphere are the surface manifestation of convective activity in the deeper layers of the sun, although the size scales of granules are much smaller than the convective plumes believed to permeate the convection zone. As well as the conspicuous granulation at the photospheric surface there is also a much larger scale 'super-granulation' which has much the same mechanism as the granules e.g, upflows at granule centre and downflows at the edges in the granular network. The flow speeds are much slower with typical speeds of 0.1 km s^{-1} . They have a much larger size of $10,000 - 30,000$ km and longer lifetimes of several days. They have an important role in the build up and concentration of magnetic flux in the intergranular lanes. Apart from, granules and supergranules, the most conspicuous features of the photosphere are sunspots. As discussed in the previous section, these are the surface manifestation of concentrated magnetic flux that has penetrated from the solar convective zone into the solar atmosphere. The spots have a temperature of ~ 4000 K, which is cooler than the typical solar

blackbody temperature of 5800 K. The spots have typical magnetic field strengths of on the order of kilo-Gauss, and have an important role to play in solar activity.

Although the intensity of the Sun in the visible may be approximated closely by a blackbody continuum, there are also the presence of dark absorption or Fraunhofer lines in the spectrum. The most notable of which are the H α and CaII H and K lines. The presence of these lines reveals that cooler part of the photosphere must overly the hotter base at $\tau_{5000} = 1$ (Phillips *et al.*, 2008). In fact, the variety of lines that are produced in the solar atmosphere (both emission and absorption) are used to determine the temperature and density stratification of the solar atmosphere. That has most notably been done in the models of (Fontenla *et al.*, 1988; Gabriel, 1976; Vernazza *et al.*, 1981), whereby a temperature and density profile of the solar atmosphere is used to calculate the emergent intensity, using radiative transfer theory. This temperature and density profile is adjusted until the modeled emergent intensities match the observed ones. The results of these models is shown in Figure 1.5. From this Figure we see that there is a temperature minimum at ~ 500 km above the photosphere where the temperature drops to ~ 4400 K. Beyond this point the temperature begins to rise again, eventually showing a rapid increase at ~ 2000 km. The region between the temperature minimum up the height at which temperature begins to rise rapidly is known as the chromosphere¹.

1.1.3.2 Chromosphere

As predicted by the models of (Fontenla *et al.*, 1988; Gabriel, 1976; Vernazza *et al.*, 1981), at ~ 500 km above the $\tau_{5000} = 1$ surface the temperature drops to a minimum of ~ 4400 K. Beyond this minimum the temperature begins to rise again, demarcating the beginning of the chromosphere. This layer of the atmosphere is generally accepted to extend to a height at which temperatures reach 20,000 K, however temperatures as high as $\sim 1 \times 10^5$ K are sometimes attributed to chromospheric heights, hence it is observable at ultraviolet (UV) wavelengths as well as visible.

¹These boundaries can vary, depending on the phenomenon observed e.g., spicules are chromospheric phenomenon which can extend far beyond the upper boundary of ~ 2000 km

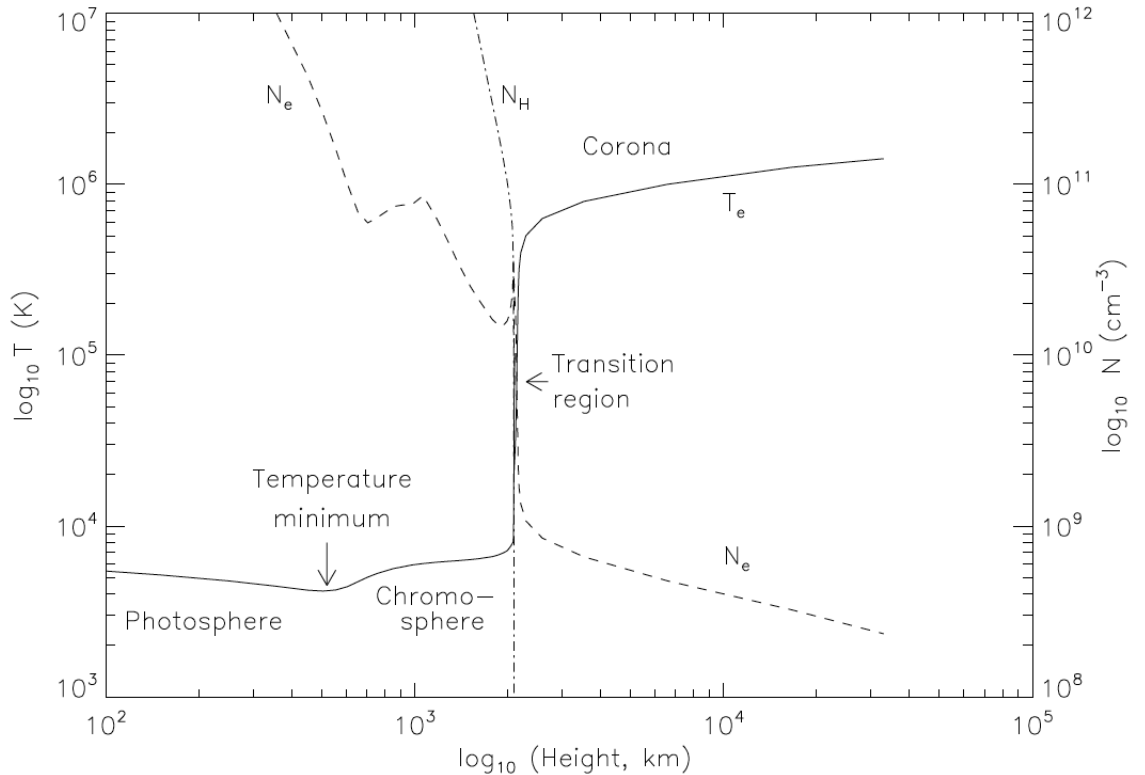


Figure 1.5: Temperature and density variation in the solar atmosphere constructed from the models of (Fontenla *et al.*, 1988; Gabriel, 1976; Vernazza *et al.*, 1981), adopted from (Phillips *et al.*, 2008).

The chromosphere is primarily observed through the Fraunhofer H α and CaII H and K lines. These lines in particular provide a good diagnostic of the chromospheric environment over a large height range since different sections of the lines are formed over various heights. By viewing the sun at or near the cores of the lines we may view different heights in the chromospheric part of the atmosphere. The chromosphere, when observed using the Ca lines, shows a highly non-uniform structured appearance. The structure is made up of dark cells with a diameter of approximately 30,000 km, with bright boundaries of the cells making up a network of bright features known as ‘the chromospheric network’. These network boundaries consisting of bright points are positions of near vertical magnetic field with a strength of 10 Gauss. This chromospheric

network is directly related to the supergranular structure as observed in the chromosphere i.e., the supergranular flows in the photosphere tend to transport field toward the boundaries of the network where they may coalesce and strengthen. These regions of strong magnetic field facilitate heating in the upper chromosphere and hence show up as regions of enhanced emission (by magnetic acoustic oscillations) in the centers of the CaII K3, for example (McAteer *et al.*, 2002). Enhanced emission in the internetwork regions (supergranule centres) show up as bright points when viewing Ca H2V and are now accepted to be formed by heat of the mid-low chromosphere by acoustic shocks (Carlsson & Stein, 1997)

Beyond the temperature minimum there is a broad temperature plateau between \sim 1000 – 2000 km, after which the temperature starts to increase dramatically. When the temperature reaches 20,000 K the extremely prominent Ly- α emission line is formed, with a wavelength of 191.5 nm, and this is accompanied by other prominent ultraviolet lines such as those of C IV, formed at temperatures of \sim 110,000 K. Such high temperatures are generally considered to be outside the range of the chromosphere and are indicative of a thin layer of the atmosphere known as the transition region. This layer is on the order of a few hundred kilometers thick but has an extremely steep temperature gradient, carrying temperatures into the mega-Kelvin range. The region of the atmosphere with temperatures greater than 1×10^6 K is known as the solar corona.

1.1.3.3 Corona

The outermost layer of the solar atmosphere is known as the solar corona, beginning at \sim 2500 km above the photosphere. It has an electron number density of 10^9 cm^{-3} at its base in quiet regions, decreasing to 10^6 cm^{-3} at distance of $1 R_\odot$ from the solar surface. The models of (Fontenla *et al.*, 1988; Gabriel, 1976; Vernazza *et al.*, 1981) reveal that beyond the transition region (\sim 2500 km) the temperature in the corona reaches well over 1×10^6 K. Such high temperatures allow the formation of emission features that belong to highly ionized heavy elements, for example Fe IX, up to as high as Fe XXIV. The presence of these highly ionized species (and many others) show that the corona has temperatures in the 1 – 2 MK range in quiet regions, active regions may exhibit temperatures

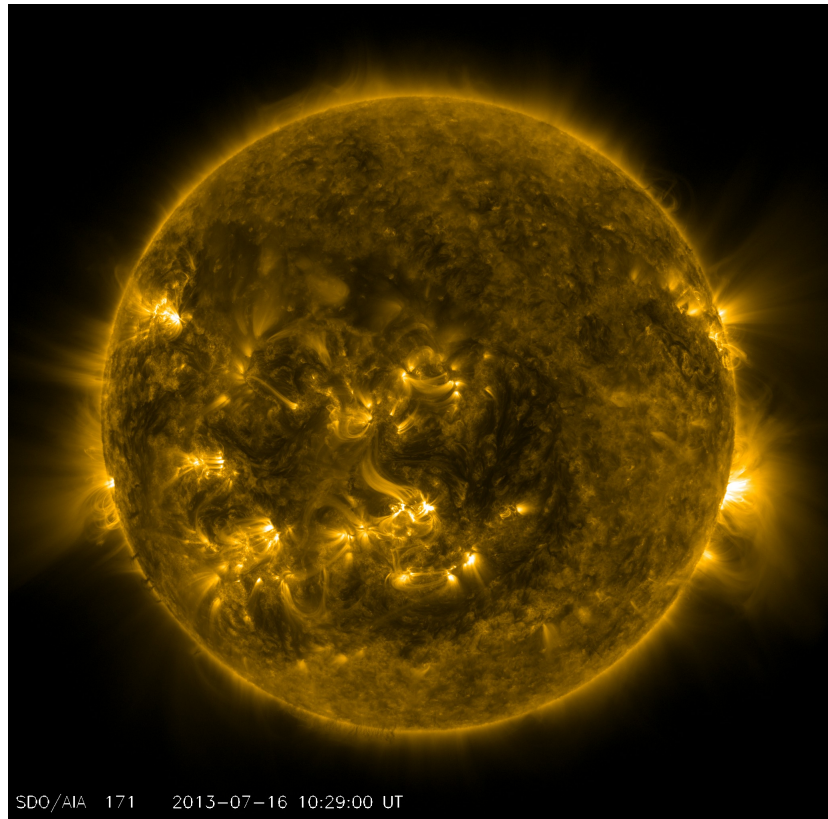


Figure 1.6: Atmospheric Imaging Assembly 171 Å image of the solar corona. Bright regions are strong concentrations of magnetic fields known as active regions (temperatures of 2 – 6 MK). Areas outside these regions are known as quiet sun (temperatures 1 – 2 MK).

in the range of 2 – 6 MK, while coronal holes may be lower than 1 MK. The temperatures of a flaring active region can be even higher than this, reaching tens of mega-Kelvin. The high temperatures and presence of highly ionized species of heavy elements means the corona is an emitter in the ultraviolet and X-ray. When viewed at these wavelengths, the corona appears highly structured, showing concentrations of bright loops known as active regions (Fig. 1.6).

Ultraviolet wavelengths allow observations of the very low corona, perhaps to only a few scale heights. However, the most extensive observations of the corona are in the visible, generally known as the 'white-light' corona. The corona's white-light radiation is primarily due to scattering of photospheric light by particles and

dust grains. The component which is due to Thomson scattering by free electrons is known as the *Kontinuierlich* or K-corona. The spectrum of this light is same as the photospheric continuum except for the absence of Fraunhofer lines. These lines are 'washed-out' of the spectrum due to thermal Doppler broadening of the high-velocity free electrons on the corona. The emission is optically thin, so the intensity is due to the number of scattering agents along the line of site. The emission is also highly polarized, depending on the line of site of the observer (we will return to this important aspect later). The K-corona dominates white-light emission from low atmosphere to $\sim 4R_\odot$. After this height, there is an increasing contribution from Rayleigh or Mie scattering from interplanetary dust grains, known as the the Fraunhofer F-corona. Since these dust grains move at a much slower velocity than the electrons, they do not wash out the Fraunhofer lines of the photospheric spectrum. The F-corona extend far beyond Earth and can be viewed in the night sky as *Zodiacal light*.

Ultraviolet and white-light observations remain the primary method of imaging the low and extended corona, respectively. However, the corona is also a strong emitter across the entire radio wavelength range, from microwave to kilometric wavelengths. Indeed, metric wavelengths provide a method of imaging the quiet and thermal corona in an optically thick regime beyond $1 R_\odot$, an ability that does not exist in white-light an UV observations.

At radio wavelengths the corona is an emitter of thermal Bremsstrahlung. Absorption via the Bremsstrahlung process, known as free-free opacity, is given by

$$\kappa_{ff} \sim \frac{n^2}{\nu^2 T^{3/2}} \quad (1.9)$$

where n is the electron density, ν is the frequency of electromagnetic radiation, and T is the temperature. Qualitatively, for a given frequency the density must drop below a certain value for this radiation to become optically thin and escape the solar atmosphere. In the radio band, even the highest frequency (microwaves) do not escape until densities drop to chromospheric values. Hence a microwave image of the sun will provide a direct observation of light escaping from this height. Reducing the frequency to metric wavelengths, the density must drop to

1.2 Coronal Mass Ejections and Coronal Shocks

coronal values before the free-free opacity is low enough for radiation to be optically thin. Hence, metric wavelength radiation escapes the solar atmosphere only in the outer corona. For example 150 MHz imaging of the solar atmosphere may image an optically thick atmosphere out to a height of $\sim 0.5 R_\odot$. The existence of an optically thick atmosphere at these wavelengths allows a direct probing of coronal temperatures at these heights. Using the solution to the radiative transfer equation

1.2 Coronal Mass Ejections and Coronal Shocks

1.2.1 CMEs

- Appearance, white-light Illing, Hundhausen, Vourlidas
- Kinematics, velocity, acceleration
- Dynamics, masses, energies, forces
- Observations at other wavelengths, EUV, radio, SXR.

1.2.2 CMEs and Shocks

- Radio bursts, Type II, Type III
- Radio imaging of shocks
- Relationship to EUV waves, Moreton waves

1.2.3 Open Questions

2

Coronal Mass Ejection and Plasma Shock Theory

2.1 Plasma Physics and Magnetohydrodynamics

2.1.1 Maxwell's Equations

$$\nabla \cdot E = \frac{\rho}{\epsilon_0} \quad (2.1)$$

$$\nabla \cdot B = 0 \quad (2.2)$$

$$\nabla \times E = -\frac{dB}{dt} \quad (2.3)$$

$$\nabla \times B = \mu_0 j + \frac{1}{c^2} \frac{dE}{dt} \quad (2.4)$$

2.1.2 Plasma Physics and Boltzmann Equation

2.1.3 Magnetohydrodynamics

2.1.4 Magnetic Reconnection

2.1.5 MHD Shocks

For acoustic shock waves there are a number of conservation equations that quantify the strength of a shock by relating the upstream gas pressure, density, flow speed, and temperature to their downstream counterparts. Such conservation equations are known as the jump conditions and the shock is considered a surface at which the fluid properties change discontinuously. The shock thickness is usually of the order of a few mean free paths of the particles in the gas, in such a case the processes in the shock surface itself are inconsequential and the relationship between upstream and downstream parameters provide a sufficient description of the shock.

When the gas is ionized and a magnetic field is present, the jump conditions must be modified to take into account the magnetic pressure and the field orientation with respect to the flow velocity and shock normal \hat{n} (unit vector normal to the shock plane). In the general case of oblique shock waves where the magnetic field direction has some arbitrary angle with respect to shock normal we may derive a set of conservation equations for the frame of the shock wave.

The flow velocity v and magnetic field B are considered to be in the xy -plane. The appropriate conservation equations are

$$[\rho v_x] = 0 \quad (2.5a)$$

$$[\rho v_x^2 + p + \frac{B_y^2}{2\mu}] = 0 \quad (2.5b)$$

$$[\rho v_x v_y - \frac{B_x B_y}{\mu}] = 0 \quad (2.5c)$$

$$[\frac{1}{2}v^2 + \frac{\gamma p}{(\gamma - 1)\rho} + \frac{B_y(v_x B_y - v_y B_x)}{\mu \rho v_x}] = 0 \quad (2.5d)$$

$$[B_x] = 0 \quad (2.5e)$$

$$[v_x B_y - v_y B_x] = 0 \quad (2.5f)$$

2.1 Plasma Physics and Magnetohydrodynamics

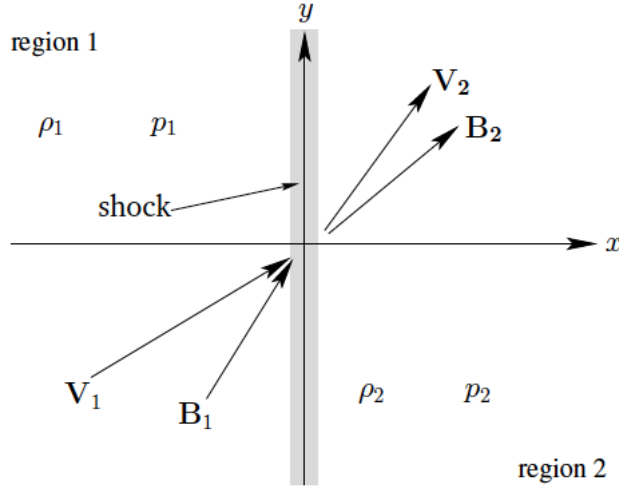


Figure 2.1: Orientation of magnetic field and velocity field with respect to shock plane, in the rest frame of the shock. Shock normal in this case would be along the $-x$ direction i.e., into upstream region 1. (Fitzpatrick, 2000)

These are the general MHD shock jump conditions where v is the fluid velocity and B is the magnetic field (with their corresponding components ‘x’ or ‘y’), ρ is the mass density, p is the thermal pressure, and γ is the ratio of specific heats (or the polytropic index). The meaning of the square brackets is $[F] \equiv F_1 - F_2$, for any quantity F , and the 1 or 2 subscripts represent upstream or downstream values of each quantity F , respectively. These set of jump conditions differ only from the purely acoustic ones due the presence of the magnetic field. For example, taking (4a), (4b), and (4d) and setting $B_x = B_y = 0$ we obtain the jump conditions for a neutral gas. Each conservation equation has a specific meaning;

- (4a) is a mass conservation equation whereby the mass flux entering the shock must equal the mass flux leaving. It has units of $\text{kg m}^{-2} \text{s}^{-1}$.
- (4b) indicates that if mass flux $\rho_1 v_{x,1}$ enters the shock with momentum $(\rho_1 v_{x,1})v_{x,1}$ it leaves the shock with momentum $(\rho_1 v_{x,1})v_{x,2}$, the difference being equal to the the changing force per unit area across the shock. In this case both thermal and magnetic pressures contribute to change in momentum flux. (4c) implies the same process but relates the x and y components

2.1 Plasma Physics and Magnetohydrodynamics

of the v and B vector fields. Both equations have units of momentum flux $\equiv (\text{kg m}^{-2} \text{s}^{-1})(\text{m s}^{-1}) = (\text{kg m s}^{-2} \text{m}^{-2}) = \text{N m}^{-2} \equiv \text{pressure}$.

- (4c) is an energy conservation term, accounting for the rate at which gas and magnetic pressure do work per unit area at the shock and equates this to the growth (or loss) in internal energy and kinetic energy across the shock. All components of magnetic field pressure are taken into in the last term on the left of the equation. All quantities are in units of $\text{J}\cdot\text{kg}^{-1}$.
- (4d) simply states that the x component of the magnetic field i.e., the component of the field that is (anti-)parallel to the shock normal \hat{n} is unaffected by the shock transition.
- (4f) relates the orientations of the upstream and downstream magnetic field to the flow speed tangential and perpendicular to the shock normal. Magnetic field orientation and hence the distribution of low speed amongst the velocity components largely depends on the whether the shock is slow-mode, intermediate, or fast mode. The equation has units of $\text{T}\cdot\text{m}\cdot\text{s}^{-1} = \text{V}\cdot\text{m}^{-1} \equiv \text{electric field}$.

4(a-f) are the general case of the jump conditions across an MHD shock, they are usually known as the MHD Rankine-Hugoniot (RH) equations. Their generality make the solution of the six unknowns from the six equations quite complicated. However the extreme cases of parallel and perpendicular shocks provide very useful and simplified expressions. It can be shown that parallel shocks i.e., $\hat{v} \parallel \hat{B} \parallel \hat{n}$ reduces to the jump conditions of a hydrodynamic shock in a neutral gas (here parallel and anti-parallel are used synonymously). The more interesting case when considering radiating shockwaves in the low solar corona is the perpendicular (or quasi-perpendicular) MHD shock, in this case the flow speed is parallel to the shock normal, and the magnetic field is perpendicular (or at a high angle) to it i.e., $\hat{v} \parallel \hat{n}$ and $\hat{B} \perp \hat{n}$. As will be shown it is this special case of quasi-perpendicular shocks that lead to efficient shock drift particle acceleration, a necessary precursor to the generation of radio emission at a coronal shockwave.

In the case of fully \perp shocks there is no need for the decomposition of the magnetic and velocity vector fields, meaning the x and y subscripts on 4(a) and

2.1 Plasma Physics and Magnetohydrodynamics

4(b) can be dropped. 4(c) is an obsolete jump condition, likewise for 4(e) since no B_x field exists. We can also rid the $B_x B_y$ terms from the last quotient in the energy conservation 4(d) –replacing it simply with $B^2/2\mu\rho$. 4(f) reduces to a simpler form of $[Bv] = 0$. Such a reduction in the generalized jump conditions allows us to express the upstream and downstream plasma properties in terms of the shock compression ratio $\chi = \frac{\rho_2}{\rho_1}$ as well as the upstream sonic Mach number $M_1 = \frac{v_1}{c_1}$ (Priest & Forbes, 2000) e.g.,

$$\frac{v_2}{v_1} = \frac{1}{\chi} \quad (2.6a)$$

$$\frac{B_2}{B_1} = \chi \quad (2.6b)$$

$$\frac{p_2}{p_1} = \gamma M_1^2 \left(1 - \frac{1}{\chi}\right) - \frac{1 - \chi^2}{\beta_1} \quad (2.6c)$$

where $\beta_1 = 2\mu p/B_1^2$ is the upstream plasma beta parameter. The exact value of the compression ratio may be obtained by using 4(b) to eliminate p from the energy flux equation 4(d) and incorporating 4(a,c,e,f) (and a lot of algebra) a quadratic for χ may be obtained

$$2(2 - \gamma)\chi^2 + [2\beta_1 + (\gamma - 1)\beta_1 M_1^2 + 2]\gamma\chi - \gamma(\gamma + 1)\beta_1 M_1^2 = 0 \quad (2.7)$$

Equation (6) has one positive real root such that

$$1 < \chi < \frac{\gamma + 1}{\gamma - 1} \quad (2.8)$$

Using a polytropic index of $\gamma = 5/3$ (monatomic) means the shock compression can be no more than a factor of 4. Another extremely important fact arising from this is that magnetic compression can also be no greater than 4 i.e., from equation 4(b) $B_2/B_1 = \chi$. $\chi < 4$ has consequences for the shock drift acceleration mechanism and may also provide an upper limit to the level of band splitting in type II radio bursts (since this effect is thought to be related to the emission induced up/downstream of the shock). Although the maximum compression ratio of 4 was derived from the roots of the quadratic for χ for the perpendicular shock, a similar analysis for the much more general oblique shock also leads to the same

2.1 Plasma Physics and Magnetohydrodynamics

result. The density compression and tangential magnetic compression can be no more than a factor of $(\gamma + 1)/(\gamma - 1)$ for any MHD shock.

Polynomials such as (6) are extremely useful, and can lead to simple expressions for the Alfvénic-Mach number in terms of χ , in this case

$$M_A = \sqrt{\frac{\chi(\chi + 5 + 5\beta)}{2(4 - \chi)}} \quad (2.9)$$

for a perpendicular shock. If the shock speed and compression ratio are known, this equation provides a means of measuring the Alfvén speed in the shock medium.

This technique is exploited in the analysis of type II radio bursts. As the shock propagates into the corona it emits EM radiation at the local plasma frequency (1) (see section 4), and since the density drops as the shock travels into the heliosphere, so too does the frequency of emission. From frequency drift rate an estimate of shock speed is possible. If band splitting of the emission is present this is interpreted as emission from upstream and downstream of the shock, which provides a diagnostic of upstream/downstream densities via (1) and hence an estimate of χ (Vršnak & Gopalswamy, 2002). However, use of (8) in calculating Mach number and Alfvén speed in the corona has some clear shortcomings such that it clearly ignores any dependency of the angle between magnetic field, velocity vector and shock normal i.e., (8) only applies to a purely perpendicular shock.

The general oblique shock case requires extra terms in the polynomial such as θ_{Bn} and θ_{vn} (θ_{Bn} is the angle between shock normal and magnetic field, and θ_{vn} is the angle between shock normal and plasma flow). For the oblique case the polynomial becomes

$$(A^2 - \chi)^2 \left[A^2 - \frac{2\chi S^2}{\chi + 1 - \gamma(\chi - 1)} \right] - \chi k^2 A^2 \left[\frac{2\chi - \gamma(\chi - 1)}{\chi + 1 - \gamma(\chi - 1)} A^2 - \chi \right] = 0 \quad (2.10)$$

where $A = \frac{M_A \cos \theta_{vn}}{\cos(\theta_{Bv} - \theta_{bn})}$, $S = \frac{c_s}{v_A}$, $k = \tan(\theta_{vn} - \theta_{Bv})$ ¹ (Kabin, 2001). Equation (6) is a quadratic of variable χ , the more general equation (9) is a cubic equation

¹ θ_{Bv} is angle between magnetic field and velocity vector, it has a simple relationship with θ_{Bn}

2.1 Plasma Physics and Magnetohydrodynamics

for χ , the roots of which give the compression for the oblique case. Since it is a function of M_A , θ_{vn} , and θ_{bv} , χ may have a range of values depending not only on Mach number but also shock orientation. Figure 2 illustrates the broad range in compressions of $0 < \chi < 3.5$ across the shock depending on both flow and magnetic field orientation with respect to the shock normal, and in this case $M_A = 2.5$. This is a very general case, however, permitting any angle of orientation of B and v . Since type II bursts are thought to be from shocks that are quasi perpendicular, this places restriction on the values for θ_{vn} , and θ_{Bn} , especially when the flow is considered to be head-on i.e. $\theta_{vn} = 0^\circ$. Therefore in the quasi-perpendicular case there is a tighter constraint on the amount of compression across the shock. Further constraining the Mach number to a limited range of values puts quite a limiting range on the compression ratio, and hence a limiting range of band splitting of type II radio bursts since $f_{plasma} \approx 9000\sqrt{n_e}$, hence

$$\delta_{bs} \equiv \frac{f_{upper}}{f_{lower}} \approx \sqrt{\frac{n_{e,d}}{n_{e,u}}} = \sqrt{\chi} \quad (2.11)$$

where $n_{e,d}$ and $n_{e,u}$ are downstream and upstream plasma number densities, and δ_{bs} is the ratio of upper to lower band frequencies, f_{upper} and f_{lower} respectively, in a split radio burst. Figure 3 shows the expected range in band splitting ($\delta_{bs} = \sqrt{\chi}$) for a type II given a range in Alfvén Mach numbers $1 < M_A < 4$, and quasi-perpendicular magnetic field orientations $45^\circ < \theta_{Bn} < 90^\circ$. This analysis shows that for a quasi-perpendicular shock the theoretically predicted range in type II band-splitting is $1 < \delta_{bs} < 1.8$. Such an upper limit to the level of band-splitting seems excessive and is probably due to a large upper limit to the Mach number being used to calculate the compression ratio. This is especially relevant in the low corona where Alfvén speed can be quite large, making it difficult for a CME or blast wave to drive a shock at $M_A = 4$. Also, given a typical band-splitting ratio of $\delta_{bs} = 1.21 \pm 0.7$ at metric wavelengths (Vršnak *et al.*, 2004), this would indicate typical Alfvén-Mach number of ~ 1.5 in the low corona. This seems reasonable, however Mach numbers of ~ 3 are possible, and figure 3 would suggest a possible band-split ratio of $\delta_{bs} \sim 1.7$ for such a Mach number. Such a level of band-splitting seems very unlikely, suggesting a quasi-perpendicular shock with a head on flow is a limiting case. More likely is a quasi-perpendicular shock with a flow

2.1 Plasma Physics and Magnetohydrodynamics

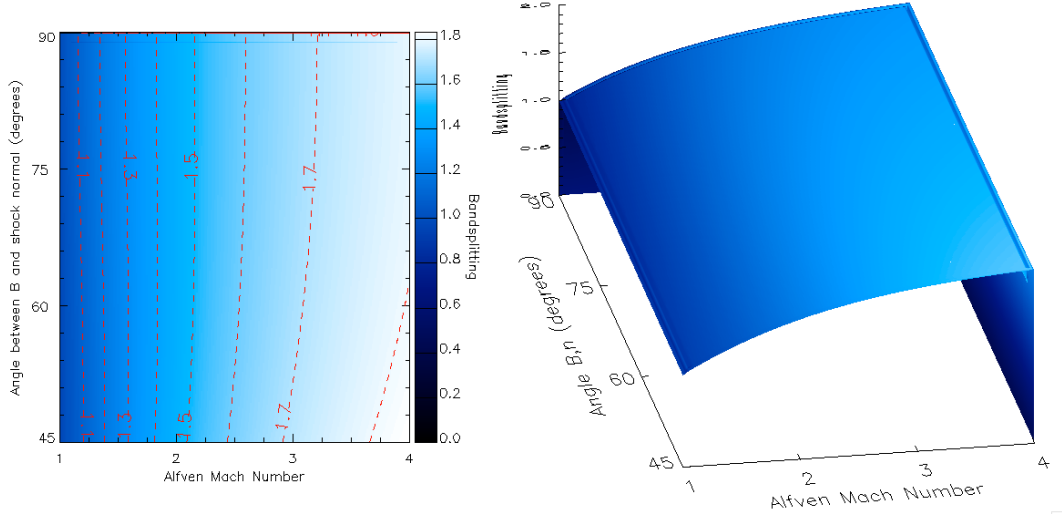


Figure 2.2: Predicted band splitting ratio δ_{bs} as a function of Mach number and magnetic field orientation with respect to shock normal. Flow is anti-parallel to shock normal (head-on). Both image and surface are shown, left and right respectively. On the left, the red contours show specific values of of band-splitting. Note that for small mach numbers the level of band splitting is independent of magnetic field orientation. It is only at Mach numbers greater than ~ 2.1 that the B-field orientation becomes important.

orientation $\theta_{vn} \neq 0$. For example if $\theta_{Bn} = 90^\circ$ and $\theta_{vn} = 45^\circ$ then band splitting can be $\delta_{bs} \sim 1.5$ for $M_A=3$, which is under the upper limit of observed type II band-split ratios of ~ 1.58 . Allowing $\theta_{vn} \neq 0$ can allow larger, more realistic Mach numbers to produce smaller and more realistic bandsplitting.

It is clear that the distribution in the level of band splitting in type II radio bursts depends not only on Mach number but the relative orientations of flow and magnetic field with respect to shock normal. A statistical analysis could possibly give an observationally predicted distribution in θ_{Bn} (provided M_A is known) that would confirm the quasi-perpendicularity of type II-generating shocks.

2.2 Coronal Mass Ejections

2.2.1 Catastrophe Model

2.2.2 Magnetic Breakout Model

The magnetic breakout model was first proposed by (Antiochos *et al.*, 1999a) and involves a quadrupolar (or more complex) magnetic flux system. A core magnetic field is flanked by two side-lobe fields, which collectively lie underneath an over-arching field that stabilizes the whole system. The overarching field and core field are almost anti-parallel, creating a magnetic null point between the two Figure 2.3. Non potentiality is injected into the core by twisting/shearing of the foot points or by flux emergence. This non-potentiality causes the core field to grow and encounter the overarching field, distorting the null point into a current sheet and eventually allowing reconnection to occur. The reconnection removes field lines from the overarching field and adds it to the side-lobe systems, allowing further growth of the core field. The growth of the core field in turn drives further breakout reconnection resulting in a positive feedback required for explosive expulsion of the core. Finally, as the core is accelerated a current sheet forms in its wake, eventually leading to a separation of the core flux from the solar surface that forms a plasmoid structure typical of a three part CME (Lynch *et al.*, 2004); an important aspect of this is that flux rope formation happens as a consequence of eruption i.e., it is not pre-existing. The magnetic breakout model was used to circumvent the Aly-Sturrock limit (Aly, 1991; Sturrock, 1991) i.e., it allowed a flux system to erupt, without having to open the constraining field lines to infinity.

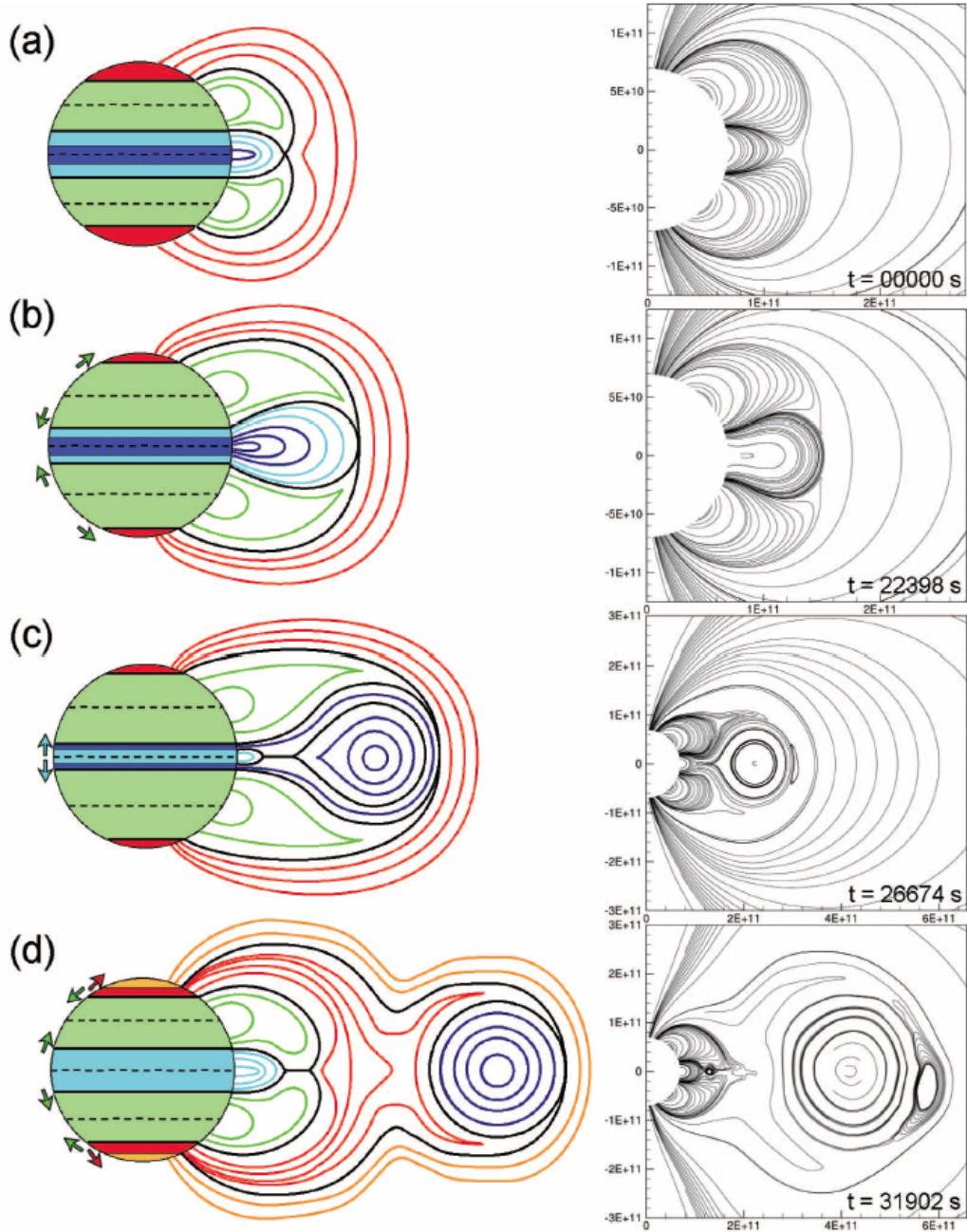


Figure 2.3: The breakout model, consisting of a quadrupolar flux system in which the central flux (blue) is flanked by two side lobe flux systems (green), with the entire system kept in stability by the tension of the overlying red field. Shearing and/or twisting on the underlying flux causes it to grow slowly. Eventually a current sheet forms at the magnetic null above the central flux, causing reconnection. This reconnection transfers overlying field to the side-lobes, effectively creating a conduit for the central flux to escape as a CME (Lynch *et al.*, 2008).

Kinematically, the CME/central field system should experience a slow rise (1 km s^{-1}) for several hours due to shearing/twisting of the foot points. Once breakout reconnection has begun the CME experiences a much larger acceleration (100 km s^{-1}). The reconnection in the current sheet in the wake of the CME is the source of energetic particles that ultimately lead to flaring (ribbons and soft x-ray loops). Therefore magnetic breakout predicts that the flaring process and SXR peak should only begin after CME acceleration (after breakout reconnection) has begun (Lynch *et al.*, 2004). However, the precedence in breakout reconnection over flaring reconnection may not always be case, with the latter sometimes driving the former (MacNeice *et al.*, 2004).

There has been observational tests of the magnetic-breakout model, showing it to be a viable explanation of some flaring and CME events, the most notable of which is the Bastille Day event (Aulanier *et al.*, 2000). The observational signatures of the model include the presence of a null point in the corona above a complex multipolar flux system (inferred from potential field source surface extrapolations), a radio source imaged to be above the erupting structure (implying a reconnection site), and radio bursts beginning at frequencies indicative of high altitude (again indicating energy release above the erupting structure, prior to eruption) (Manoharan & Kundu, 2003a). However, in some instances magnetic breakout is implied by observations of the above, but the kinematics are inconsistent with model predictions. For example the model predicts a long slow rise of the central flux system as the underlying field is increasingly sheared, after which there is a rapid acceleration once breakout reconnection is initiated. However, in the study of Bong *et al.* (2006) the breakout reconnection occurred at the end of the CME acceleration phase, prompting a two-phase acceleration scenario.

2.2.3 Toroidal Instability

The toroidal instability model incorporates a pre-existing flux rope structure that is built from a torus of magnetic flux, some of which is buried beneath the photosphere (Chen, 1989). The flux system is can be broken down into a combination of toroidal magnetic, toroidal current and a poloidal magnetic field and current Figure 2.4. This flux rope system is embedded in a surrounding coronal magnetic

field B_{corona} . The stability of the system depends on the nature of the $J \times B$ force due to the interaction toroidal and poloidal components of both the field and current. The interaction of J and B internal to the flux rope is usually termed the Lorentz self-force or the ‘hoop’ force. An instability may be induced via twisting of the fluxrope footpoints to increases the amount of poloidal flux (effectively increasing the helicity of the system). The instability arrises when the outward hoop force deccreses more slowly within the ring radius than the opposing Lorentz force due to an external magnetic field. Once the instability is induced, the fluxrope begins a bulk motion as well as a growth in its semi-minor axis. Hence the motion of the system can be analysed by looking at the central axis or the minor axes (leading and trailing edges. The three axes display slightly different kinematics e.g., the leading edge has a faster velocity than the trailing edge (due to fluxrope expansion). this has proved a useful test of the model when comparing the observations of erupting fluxrope structures as seen in white-light coronagraphs. Krall *et al.* (2001) looked at the leading a trailing edges of erupting flux ropes, as well as the rope aspect ratio, an compared the observations to model expectations. Good agreement is found between the model kinematics and aspect ratio and the observed events. The equation of motion of the entire system is given by

$$M \frac{d^2Z}{dt^2} = \frac{I_t}{c^2 R} \times \left[\ln\left(\frac{8R}{a}\right) - 1 + \frac{\xi_i}{2} + \frac{\beta_p}{2} - \frac{B_t^2}{B_{pa}^2} - \frac{2RB_{\perp c}}{aB_{pa}} \right] - F_g - F_{drag} \quad (2.12)$$

where I_t is the toroidal current, R is the flux rope major radius, a is the rope minor radius, ξ_i is internal inductance of the flux system, B_t is the toroidal field, B_{pa} is the poloidal field at a , $B_{\perp c}$ is the perpendicular component of the ambient coronal field, F_g is the force due to gravity, F_{drag} is the drag force, M is the mass per unit length of the rope, and Z is the rope axis height above the photosphere. The equation of motion shows that an increase in the toroidal current (or poloidal flux) contributes positively to the acceleration. The terms in the square brackets are each unitless and take into account the rope geometry, self-inductance and interplay between poloidal and toroidal flux. The first three terms in the square brackets are what give rise to the hoop-force. If the rope is mass loaded with a prominence, this can contribute to the rope’s stability via the gravity term. The

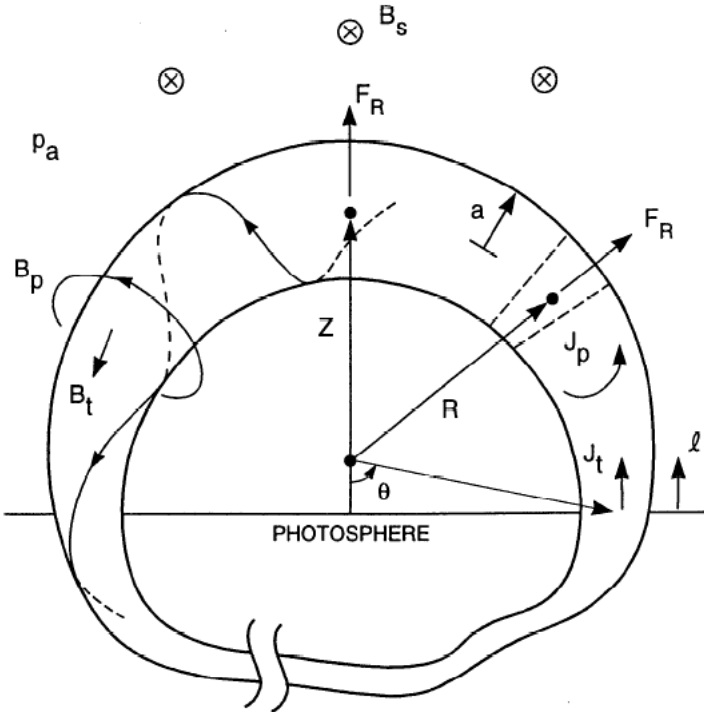
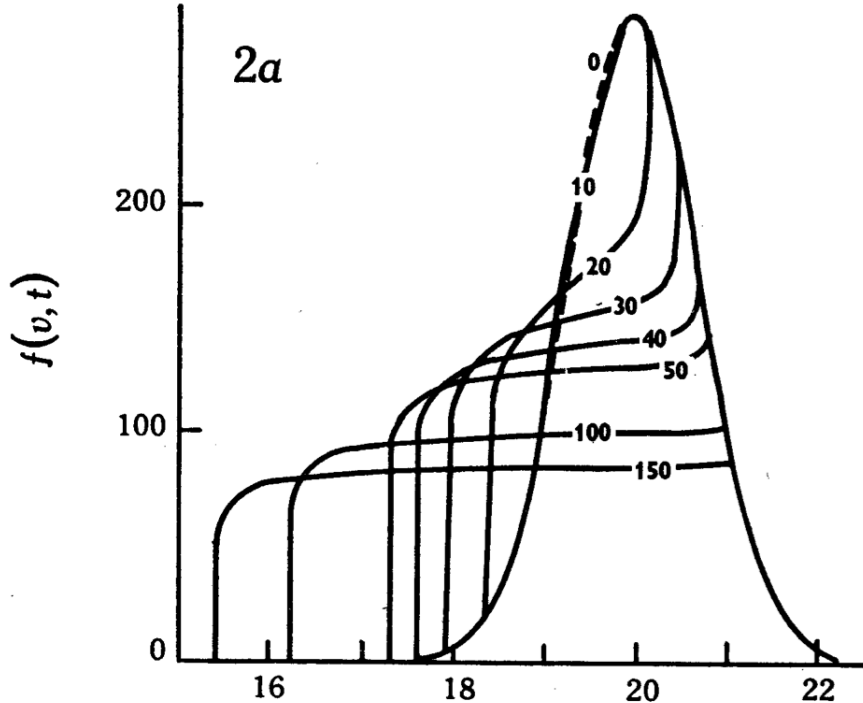


Figure 2.4: The flux rope model of Chen (1989), used to study the toroidal instability of a twisted flux system in the corona.

drag term only becomes an important contributor to rope dynamics later in the propagation, when the solar wind speed begins to increase i.e., at around $10R_{\odot}$ reference Sheeley. The eruption is driven by flux-injection, which typically lasts for 4-8 hours, during which time the unstable system loses its equilibrium and begins to rise Krall *et al.* (2001).

It is significant the fluxrope is already established in the corona before eruption begins i.e., the rope formation is not addressed in the model and it is not a consequence of eruption. Hence magnetic reconnection is not a necessary aspect of the model and the eruption may proceed without employing resistive MHD. The model has been tested against observations and found to provide consistent result with the acceleration and jerk profiles of destabilized filaments during eruption (Schrijver *et al.*, 2008a)



2.2.4 Drag Models

2.3 Coronal Shocks and Plasma Emission

2.3.1 Shock Particle Acceleration

2.3.2 Wave-Particle Interaction

Quasi-linear relaxation

2.3.3 Three-Wave Interaction and Plasma Emission

Once the Langmuir waves are produced from the bump-on-tail instability a number of wave interaction processes occur in order to bring about plasma emission. This involves the interaction of various wave modes in the plasma described by a mathematical formalism called the three-wave interaction. In this process three wave modes in a plasma M, P, and Q are described by their distribution functions in a wave-number space (k -space). the distribution functions are given by

2.3 Coronal Shocks and Plasma Emission

$N_M(k_M)$, $N_P(k_P)$, $N_Q(k_Q)$, where the N describe the occupation number of wave quanta between k and $k + dk$ in the wave-number space. Waves in P and Q mode may interact to such that wave quanta are removed from the P and Q k-space and added to the M k-space. This is essentially an emission of an energy packet from the P and Q -space to the M k-space. The rate of change of occupation numbers in the three k-spaces are given by

$$\frac{dN_M(\mathbf{k}_M)}{dt} = - \int \frac{d^3\mathbf{k}_P}{(2\pi)^3} \int \frac{d^3\mathbf{k}_Q}{(2\pi)^3} g(\mathbf{k}_M, \mathbf{k}_P, \mathbf{k}_Q) \quad (2.13)$$

$$\frac{dN_P(\mathbf{k}_P)}{dt} = - \int \frac{d^3\mathbf{k}_M}{(2\pi)^3} \int \frac{d^3\mathbf{k}_Q}{(2\pi)^3} g(\mathbf{k}_M, \mathbf{k}_P, \mathbf{k}_Q) \quad (2.14)$$

$$\frac{dN_Q(\mathbf{k}_Q)}{dt} = - \int \frac{d^3\mathbf{k}_M}{(2\pi)^3} \int \frac{d^3\mathbf{k}_P}{(2\pi)^3} g(\mathbf{k}_M, \mathbf{k}_P, \mathbf{k}_Q) \quad (2.15)$$

where $g(\mathbf{k}_M, \mathbf{k}_P, \mathbf{k}_Q)$ is incorporates a transition probability for wave quanta into and out of energy states in the various k-spaces (Robinson *et al.*, 1994). The transition probability is given by

$$g(\mathbf{k}_M, \mathbf{k}_P, \mathbf{k}_Q) = u_{MPQ}(\mathbf{k}_M, \mathbf{k}_P, \mathbf{k}_Q) [N_M(\mathbf{k}_M)N_P(\mathbf{k}_P) - N_P(\mathbf{k}_P)N_Q(\mathbf{k}_Q) + N_Q(\mathbf{k}_Q)N_M(\mathbf{k}_M)] \quad (2.16)$$

where $u_{MPQ}(\mathbf{k}_M, \mathbf{k}_P, \mathbf{k}_Q)$ is the transition probability from states in P and Q to M, for example (Melrose, 1986). u_{MPQ} is analogous to transition probabilities given by the Einstein coefficients for transferring energy packets from and atomic state to a photon state (photon emission) i.e., whereas the Einstein coefficients are used in atom-wave (atom-photon) energy exchanges, u_{MPQ} describes wave-wave energy exchanges. The transition probability is given by

$$u_{MPQ}(\mathbf{k}_M, \mathbf{k}_P, \mathbf{k}_Q) \propto \delta(\omega_M - \omega_P - \omega_Q) \delta^3(\mathbf{k}_M - \mathbf{k}_P - \mathbf{k}_Q) \quad (2.17)$$

where the ω are the frequency of the corresponding wave and and δ are delta functions. Given the presence of delta functions in the transition probability expression, we can see that an exchange of energy quanta amongst the wave

2.3 Coronal Shocks and Plasma Emission

modes can only occur when

$$\omega_M = \omega_P + \omega_Q \quad (2.18)$$

$$\mathbf{k}_M = \mathbf{k}_P + \mathbf{k}_Q \quad (2.19)$$

Hence for an a conversion wave modes in a plasma such as $M \rightarrow P + Q$ (a decay of mode M into P and Q), or it's reverse process $P + Q \rightarrow M$ (a coupling of P and Q to produce M) is described by equations (2.1) to (2.7).

The production of plasma emission after a bump-on-tail instability has occurred requires a three wave interaction amongst a Langmuir wave L , ion acoustic wave S , and electromagnetic wave T . Fundamental emission during a radio burst occurs via a decay of Langmuir waves into an electromagnetic and ion sound wave

$$L \rightarrow T + S \quad (2.20)$$

while second harmonic first requires the decay $L \rightarrow L' + S$, where L' is a product Langmuir wave propagating in the opposite direction to the first. This is followed by a coalescence of the original and product Langmuir waves

$$L + L' \rightarrow T' \quad (2.21)$$

- The dispersion relations
- Source emissivities

3

Observation and Instrumentation

3.1 Thompson Scattering Theory

3.1.1 Thomson Scattering in the Corona

The first evidence for the existence of the corona was through observations during solar eclipses. The occultation of the solar disk by the moon revealed a visible outer atmosphere structured into streamers and plumes and extending far from the solar surface (Fig. ??). This is known as the white-light corona and is due to Thomson scattering of photospheric light by free electrons in the corona.

The tangential component (I_T), radial component (I_R), and polarization (I_P) of the scattered intensity are given by the expressions

$$I_T = I_0 \frac{\pi \sigma_e}{2z^2} [(1-u)C + uD] \quad (3.1)$$

$$I_P = I_0 \frac{\pi \sigma_e}{2z^2} \sin^2 \chi [(1-u)A + uB] \quad (3.2)$$

with $I_R = I_T - I_P$. A , B , C , and D are the van de Hulst coefficients and are a trigonometric function only of the solid angle subtended by the Sun at the scattering point (see Appendix). I_0 is incident intensity, σ_e is the electron

3.1 Thompson Scattering Theory



Figure 3.1: The white-light corona during a solar eclipse. Occultation of the bright solar disk by the moon reveals the faint outer atmosphere of the Sun, known as the corona. It is highly structured, showing features like streamers and plumes. *Eclipse photograph courtesy of Miloslav Druckmüller <http://www.zam.fme.vutbr.cz>*

scattering cross section, z is the distance from scatterer to observer, u is a limb darkening coefficient, and χ is the angle between a radial vector from sun centre to the scattering electron and a position vector from observer to the electron.

The total scattered intensity is given by

$$I_{tot} = 2I_T - I_p \sim I_0 \frac{\pi \sigma_e}{z^2} \left(1 - \frac{\sin^2 \chi}{2} \right) \quad (3.3)$$

The van de Hulst coefficients are solutions of a set of integrals to obtain the brightness of each component of the radiation scattered by a single electron in the solar corona. They are a result of scattering theory applied to the case of an electron receiving radiation from the entire solar disk, as opposed to a simpler

3.1 Thompson Scattering Theory

point source of incident radiation. They are as follows

$$A = \cos \Omega \sin^2 \Omega \quad (a)$$

$$B = -\frac{1}{8} \left[1 - 3 \sin^2 \Omega - \frac{\cos^2 \Omega}{\sin \Omega} (1 + 3 \sin^2 \Omega) \ln \left(\frac{1 + \sin \Omega}{\cos \Omega} \right) \right] \quad (b)$$

$$C = \frac{4}{3} - \cos \Omega - \frac{\cos^3 \Omega}{3} \quad (c)$$

$$D = \frac{1}{8} \left[5 + \sin^2 \Omega - \frac{\cos^2 \Omega}{\sin \Omega} (5 - \sin^2 \Omega) \ln \left(\frac{1 + \sin \Omega}{\cos \Omega} \right) \right] \quad (d)$$

where Ω is the angle between the lines QS and QT. Q is the scattering point, S is Sun center, and T is the point where the scattered point vector crosses the Sun at a tangent (Howard & Tappin, 2009a).

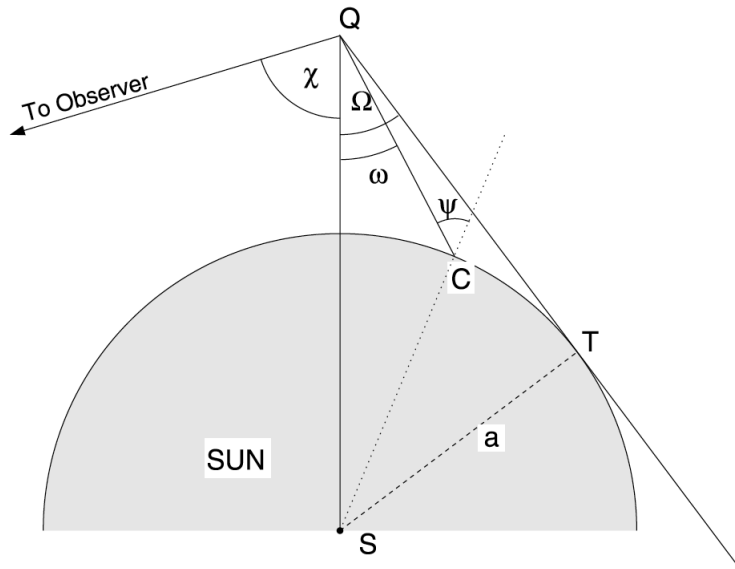


Figure 3.2: Geometry of single electron scattering in the solar atmosphere, with angles Ω and χ .

3.1.2 White-light observations of CMEs

3.2 Coronagraphs

Before the early 20th century the only way to view the corona was for a short period during a solar eclipse when the moon blocks direct photospheric light. Under normal conditions direct sunlight overwhelms the faint corona. In 1939 the French Astronomer Bernard Lyot developed a telescope, known as a coronagraph, which allowed observation of the corona at any time (Lyot, 1939). A coronagraph is an optical system that provides an artificial eclipse of direct photospheric light so the much fainter corona can be imaged.

3.2.1 Lyot Coronagraph

The Lyot Coronagraph is the name given to the first optical design of a coronagraph developed by Bernard Lyot. A basic schematic of the instrument is given in Figure 3.3. The optical element O1 is a lens that is extremely polished to prevent scattering and reflections of incident light. O1 creates an image of the Sun onto its focal plane at F1 where the occulting disk, D1, reflects away the unwanted solar disk image. F1 then images the objective lens and the occulting disk onto the plane of O2. Lyot's key invention was the Lyot stop and Lyot spot. These are devices onto which light diffracted at the occulting disk is directed and subsequently blocked from being imaged by the final lens O2. O2 then images the faint corona and occulting disk onto the detector plane.

The Lyot coronagraph is described as internally occulting due to the placement of the occulting disk behind the first objective lens. This is to distinguish it from an externally occulted system in which the disk is placed in front of the objective lens. Modern coronagraphs follow the same basic design of Lyot's but contain extra features such as baffles to stop any scattered light in the telescope.

3.2.2 STEREO COR1 and COR2

The *Solar Terrestrial Relations Observatory* (STEREO; Kaiser *et al.*, 2008) Ahead and Behind are two nearly identical spacecraft traveling ahead and behind Earth in its orbit. Each spacecraft is receding from Earth at a rate of $\pm 22^\circ$ per year, such

3.2 Coronagraphs

INTERNALLY OCCULTED REFRACTING CORONAGRAPH (LYOT)

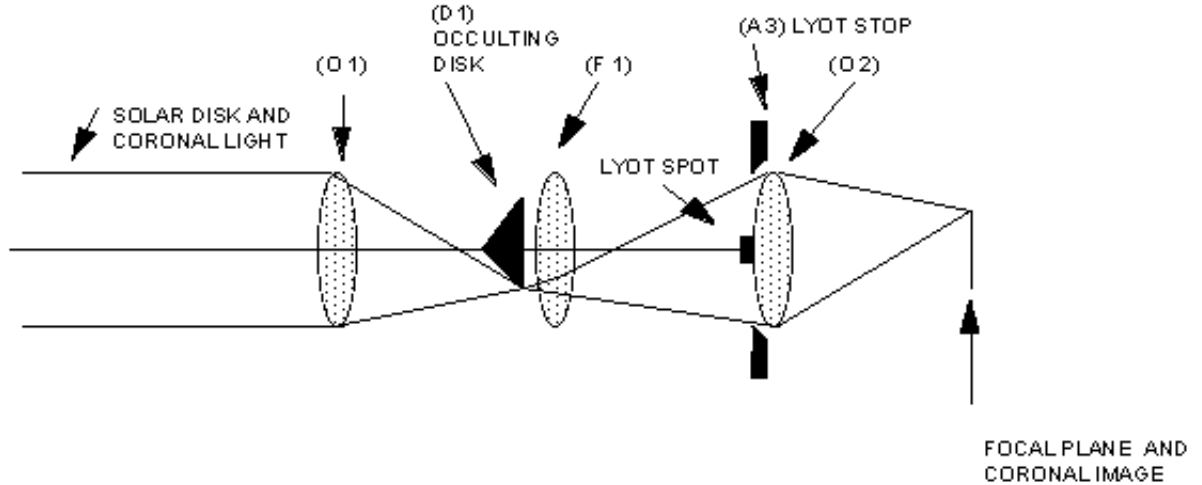


Figure 3.3: A schematic of the basic optical design of the Lyot coronagraph. Lyot's key inventions were the placement of a Lyot stop and Lyot spot at the positions where diffracted light would contaminate the image and obscure the faint corona.

that they are effectively traveling around the Sun in opposite directions. They carry an identical set of instruments known as the Sun Earth Coronal Connection and Heliospheric Investigation (SECCHI) suite, including in situ detectors and a variety of imagers. On each spacecraft there are two coronagraphs, COR1 and COR2 (Howard *et al.*, 2008). The Ahead COR1 and COR2 combined with Behind COR1 and COR2 offer a stereoscopic view of the corona and any transient event taking place, such as a CME.

COR1 is an internally occulted Lyot coronagraph, see Figure 3.4. It images the inner corona with a field of view from $1.4 - 4.5 R_{\odot}$ in a waveband 22.5 nm wide centered on the H α line at 656 nm. It has an internal polarizer that takes three images at 0° , 120° , and 240° , so that polarized or total brightness images of the inner corona may be produced. It nominally produces 1024×1024 pixel images with platescale of 3.75 arcsec per pixel (Thompson & Reginald, 2008). A typical observing sequence will give an image cadence of 10 minutes.

COR2 is an externally occulted Lyot coronagraph. Externally occulted coron-

3.3 Radio Spectrometers and Radioheliographs

ographs have an extra occulting disk in front of the objective lens, see Figure 3.5. This is to prevent direct sunlight scattering off of the objective lens, making internally scattered light less of a problem for this type of coronagraph. A downside to this design is that the external occulter does not allow the inner corona to be imaged, hence such coronagraphs are usually used to observe the extended corona to larger heights. COR2 observes the corona in a field of view from $2.5 - 15 R_{\odot}$ and in a wavelength range of 650 – 750 nm. It nominally produces 2048×2048 images, with 14.7 arsec per pixel. Like COR1 it has an internal polarizer producing three linearly polarized images per observing sequence (30 minutes).

These white light imagers of the corona allow for a stereoscopic view of CMEs in a total field of view covering $1.4 - 15 R_{\odot}$. The two viewpoint capabilities of these telescopes offer a more accurate observational estimation of both CME kinematics and CME mass, resulting in a better understanding of CME dynamics.

3.2.3 SOHO LASCO

3.3 Radio Spectrometers and Radioheliographs

3.3.1 RSTO Callisto

3.3.2 STEREO WAVES

3.3.3 Nancay Decametric Array

3.3.4 Nancay Radioheliograph

3.4 EUV imaging

3.4.1 SDO AIA

3.4 EUV imaging

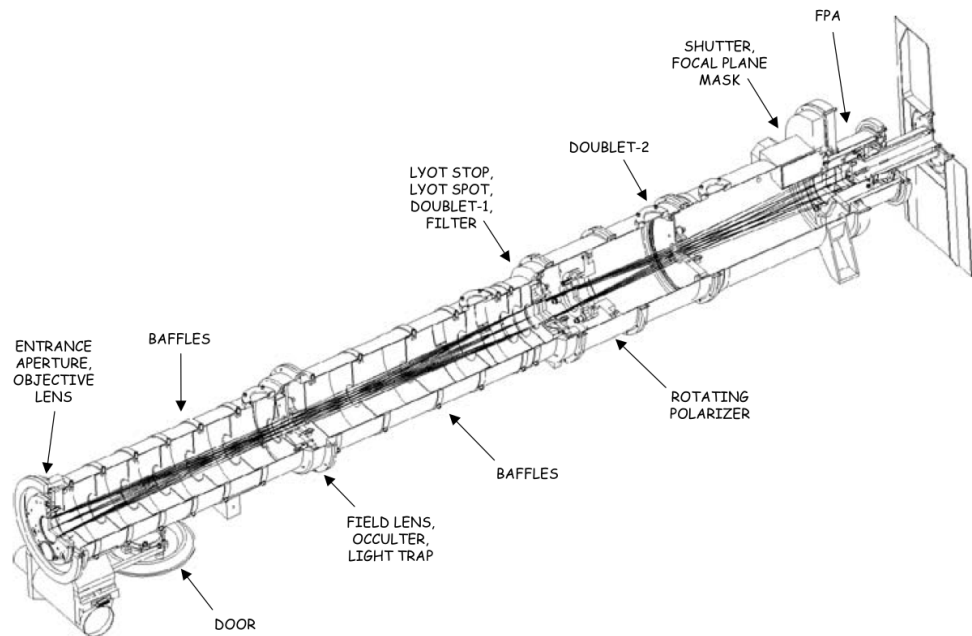


Figure 3.4: A schematic of the basic optical design of the the COR1 coronagraph. There are two such identical instruments, one on the Ahead and one on the Behind spacecraft. It is the same basic design as the Lyot coronagraph with the addition of baffles to prevent scattered light and a polarizer behind the Lyot stop (Thompson & Reginald, 2008).

3.4 EUV imaging

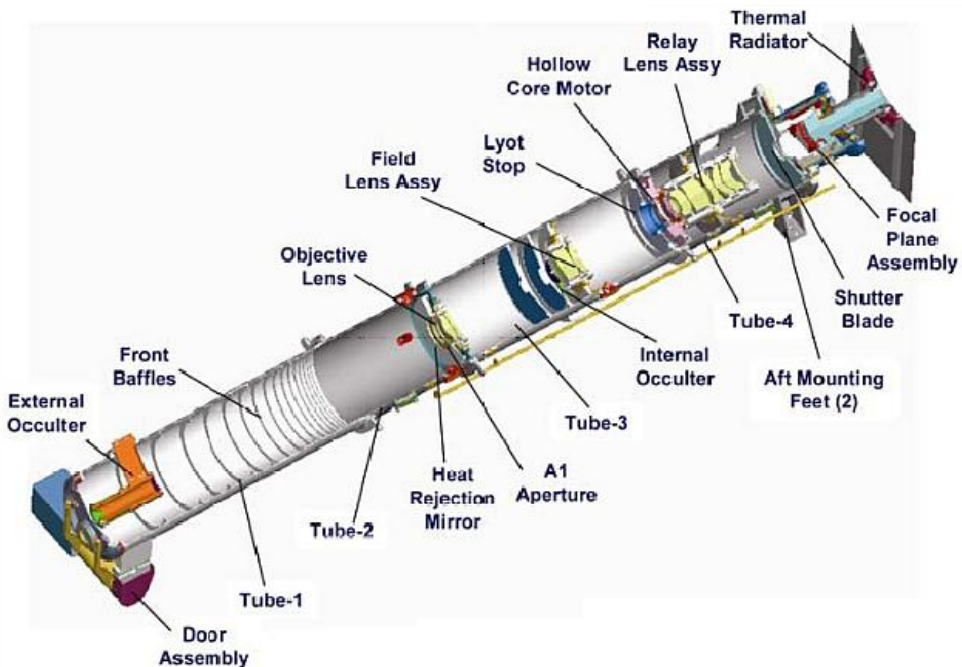


Figure 3.5: A schematic of the basic optical design of the COR2 coronagraph. This is an externally occulted coronagraph, meaning it has an extra occultation disk in front of the objective lens. This results in less internally scattered light, but also results in an obscuration of the inner corona. As with COR1, there are two such identical instruments, one on the Ahead and one on the Behind spacecraft (Howard *et al.*, 2008).

4

Coronal Mass Ejection Masses, Energetics, and Dynamics

4.1 Masses

Despite many years of study, the origin of the forces that drive coronal mass ejections (CMEs) in the solar corona and interplanetary space are not well understood. From an observational viewpoint a complete understanding of CME kinematics, dynamics and forces requires not only a study of CME speed, acceleration and expansion but also an accurate knowledge of CME mass. The measurements of CME mass combined with acceleration measurements can be used to quantify the magnitude of the force that drives a CME. Knowledge of this force magnitude can lead to an identification of the possible origin of the CME driver.

There are numerous theoretical models that attempt to explain the triggering of CME eruption and its consequent propagation. Each describe the destabilization and propagation of a complex magnetic structure, such as a flux rope, via mechanisms that include the catastrophe model (Forbes & Isenberg, 1991; Forbes & Priest, 1995; Lin & Forbes, 2000), magnetic breakout model (Antiochos *et al.*,

1999b; Lynch *et al.*, 2008), or a toroidal instability model (Chen, 1996; Kliem & Török, 2006). The loss of equilibrium induced by such mechanisms results in CME propagation into interplanetary space. The predictions of these models have been investigated in observational studies whereby the CME kinematics are used to constrain what forces might be at play and hence which model best describes CME propagation. Such studies show that early phase propagation can be reasonably described by the existing models (or a combination of them) involving some form of magnetic CME driver (Chen *et al.*, 2006; Lin *et al.*, 2010; Manoharan & Kundu, 2003b; Schrijver *et al.*, 2008b), and that aerodynamic drag of the solar wind may have a significant role at later stages of CME propagation (Byrne *et al.*, 2010; Howard *et al.*, 2007; Maloney & Gallagher, 2010). Comparisons between modeling and observational estimates of the forces that drive CMEs requires an accurate determination of CME kinematics properties as well as CME mass.

To date, the most prevalent method of determining CME mass has been through the use of white light coronagraph imagers, such as the Large Angle Spectroscopic Coronagraph (LASCO; Brueckner *et al.*, 1995) on board the *Solar and Heliospheric Observatory* (*SOHO*; Domingo *et al.*, 1995) and the twin Sun Earth Connection Coronal and Heliospheric Investigation (SECCHI) COR1 and COR2 coronagraphs (Howard *et al.*, 2008) on board the *Solar Terrestrial Relations Observatory* (*STEREO*; Kaiser *et al.*, 2008). The white-light emission imaged by such coronagraphs occurs via Thomson scattering of photospheric light by coronal electrons (Billings, 1966; Minnaert, 1930; van de Hulst, 1950), the so called K-corona. From classical Thomson scattering theory, the intensity of the light detected by an observer depends on the particle density of the scattering plasma. Hence, any density enhancement, such as a CME, over the background coronal density appears as enhanced emission in white light. The enhanced emission allows for a calculation of the total electron content and hence mass.

Some of the first measurement of CME mass using scattering theory were carried out by Munro *et al.* (1979) and Poland *et al.* (1981) using space-based white light coronagraphs on board *SkyLab* and U.S. military satellite *P78-1*. Both the early studies and later statistical investigations determined that the majority of CMEs have masses in the range of 10^{13} – 10^{16} g, (Vourlidas *et al.*, 2002, 2010).

However, due to only a single viewpoint of observation, the longitudinal angle at which the CME propagates outwards was largely unknown in these studies and it is generally assumed that the CME propagates perpendicular to the observers line-of-sight (LOS). There is also the added assumption that all CME mass lies in the two-dimensional plane-of-sky (POS). Such assumptions can lead to a mass underestimation of up to 50% or more (Vourlidas *et al.*, 2000). More recent studies have employed the two viewpoint capabilities of the *STEREO* mission to determine the mass of numerous CMEs with much less uncertainty (Colaninno & Vourlidas, 2009).

In this paper, we analyze mass development of the 2008 December 12 CME using the *STEREO* COR1 and COR2 coronagraphs. We use a well constrained angle of propagation to determine the mass and position of the CME. Combining the mass measurements with values for CME velocity and acceleration, the kinetic energy and the magnitude of the force influencing propagation is determined for each point in time. Section 2 describes the observations of the event from first appearance of the front in COR1 A and B to the time when the front exits the COR2 A and B fields of view. Section 3 describes the methods by which the mass, energy, and force are calculated with *a priori* knowledge of the propagation angle. Section 4 includes the results and Section 5 discusses the possible forces attributable to the observed accelerations and whether they are magnetic or aerodynamic in origin. This is followed by conclusions in Section 6.

4.1.1 Observations

The COR1 images used in this analysis span from 2008 December 12 04:05 UT to 15:45 UT, with a cadence of 10 minutes. The three polarization states of COR1 were combined to make total brightness images in units of mean solar brightness (MSB). Base difference images were produced using the 04:05 UT image (in both COR1 A and B) as a background to be subtracted from all subsequent images. A sample of such images for both COR1 A and B can be found in Figure 4.1. The COR2 images analyzed range from 07:22 UT to 17:52 UT, with a cadence of 30 minutes. As with the COR1 images, total brightness images were created for COR2, and a set of base difference images were then produced using the

4.1 Masses

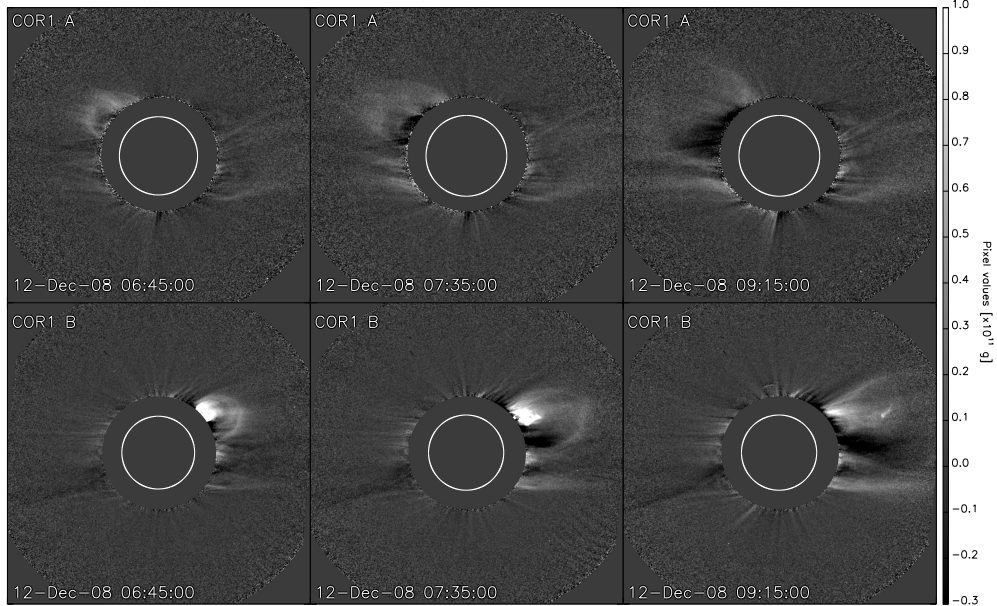


Figure 4.1: Selection of base difference images of the CME in COR1 A (top row) and COR1 B (bottom row), with pixel values of grams. The CME is quite faint in the A images and appears not to have as much structure as in B. There is a large contribution to mass from a near-saturated region to the upper flank of the CME in the B images. Such saturation in the mass images coincides spatially with the prominence in total brightness images.

07:22 UT image as a suitable background. A selected set of images from COR2 can be found in Figure 4.2.

At 04:35 UT the leading edge of a CME appeared in COR1 A and B coronagraphs at a height of $\sim 1.4 R_{\odot}$, off the east and west limb respectively. In COR1 B the CME first appears as a set of rising loop-like structures followed by a prominence, part of which appears to fall back to the surface at 08:00 UT while the remainder was ejected and follows the rising loop-like structures which eventually become the CME front. The rising prominence was not apparent at any stage of the propagation in COR1 A and the advancing front remains the only distinguishable facet of the CME from this line-of-sight (LOS).

A noteworthy caveat of using base difference imaging is the assumption that the background corona in the pre-event image has the same brightness in all subsequent images. This may not always be true and any excess brightness in the pre-event image will produce negative pixel values in the base difference. This is

4.1 Masses

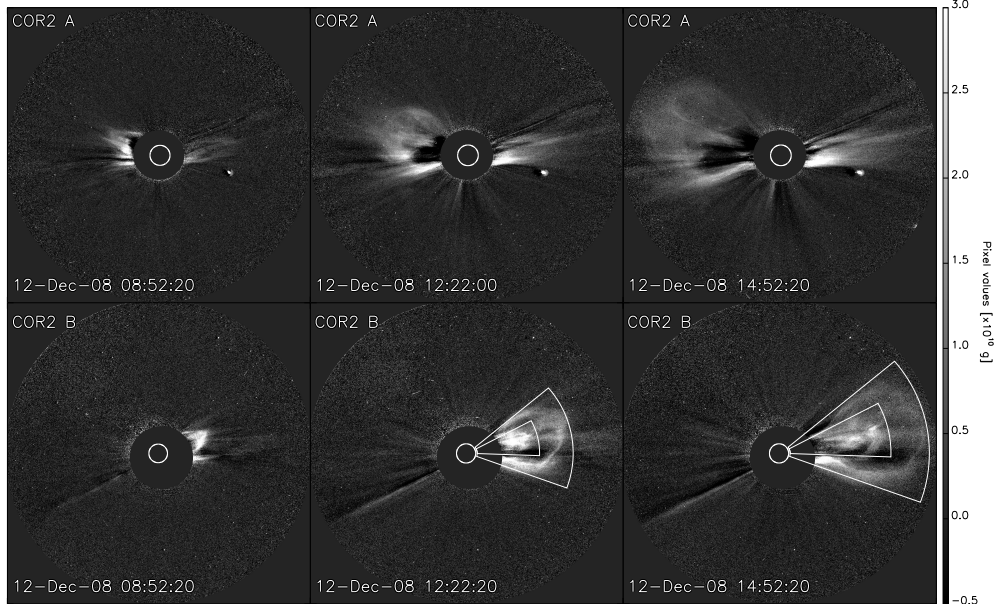


Figure 4.2: Selection of base difference images of the CME in COR2 A (top row) and COR2 B (bottom row), with pixel values of grams. The CME is clearly distinguishable in both fields of view. Only the B field view shows clearly the three part structure of core, cavity and front. The COR2 B images were used to measure core and front mass separately

apparent in the COR1 images as the CME interacts with a streamer, displacing it as the leading CME front expands laterally as well as moves outward. The streamer is visible as a dark feature that grows with time at the southward flank of the CME in the COR1 B images, Figure 4.1. The black areas are indicative of negative pixel values. The COR1 A images also suffer from negative pixels, especially at later times, see Figure 4.1 top row, 09:15 UT image. The front of the CME starts to exit both the A and B field of view at \sim 08:35 UT.

The CME first appears in the COR2 field of view at \sim 07:52 UT with the CME apex at a height of $\sim 3 R_{\odot}$ in both A and B images. In the B coronagraph, by 10:52 UT the three part structure of core, cavity, and bright front is clearly visible and the overall structure grows in size as the CME propagates to larger heights. The core becomes more tenuous and the mass distribution becomes homogenous after 15:52 UT when the front starts to exit the field of view. The distinction between core and front is not as clear in COR2 A and the mass distribution ap-

pears more homogenous throughout the propagation. As with the COR1 images, COR2A is also affected by excess brightness in the pre-event image, as is apparent by a growing dark feature in its southern half. As the pre-event image for COR2B is the cleanest of the pre-event images (it contains the least contamination by streamers), the COR2B data are considered the best candidate for accurate CME mass measurements.

4.1.2 Evaluation of Uncertainties

The method by which mass measurements are derived from white light coronagraph images is based on theory first developed by Minnaert (1930) in which the scattering geometry of a single electron at a particular point in the solar atmosphere is considered. Further development of the theory by van de Hulst (1950) led to the derivation of what are now known as the van de Hulst coefficients. The coefficients treat each component of the incident electric field vector separately and take into account the finite size of the solar disk (Billings, 1966; Howard & Tappin, 2009b; Minnaert, 1930). An important fact arising from these expressions is the dependence of scattering intensity on the angle, χ , between the radial vector from sun centre to the scattering electron and a position vector from observer towards the electron—the LOS, see Figure 4.3. Scattering efficiency is minimized when this angle is 90° . However, along the LOS such an angle occurs at the point of minimum distance from sun centre where the incident intensity (that the electron receives) and electron density are maximized. This means scattered light in the corona is most intense along a plane perpendicular to the observer’s LOS despite the efficiency of scattering being minimized at such viewing angles (Howard & Tappin, 2009b). This plane perpendicular to the LOS is known as the plane-of-sky (POS)

Studies using single LOS coronagraph data are often hindered by the unknown CME propagation angle from the POS, e.g., unknown θ (or χ) in Figure 4.3. This leads to the incorrect angle being used when inverting the van de Hulst coefficients to calculate the number of electrons contributing to the scattered light. Furthermore, because the 3-D extent of the CME is unknown it is also

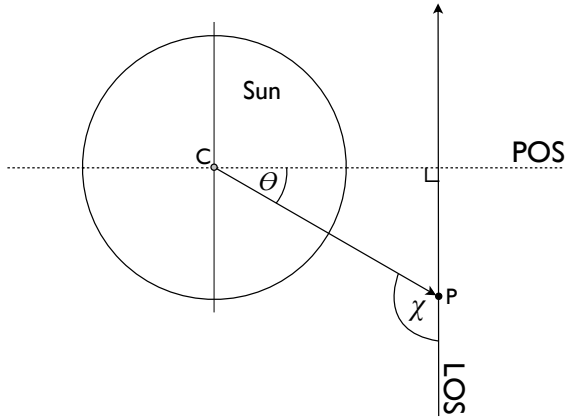


Figure 4.3: Schematic showing the relative orientation of the line-of-sight (LOS), and the plane-of-sky (POS). Electron position is at point P and C is Sun center. The vector CP may also represent CME propagation direction. Scattering efficiency is heavily dependent on the angle θ (or χ) and is least efficient when $\theta = 0^\circ$ ($\chi = 90^\circ$).

assumed that the CME is confined to the 2-D sky plane, leading to a significant CME mass underestimation (Vourlidas *et al.*, 2000).

The CME of 2008 December 12 was Earth-directed (Byrne *et al.*, 2010), making it roughly the same angular distance from both the *STEREO* A and B spacecraft, then located ± 45 degrees from Earth. This known angle of propagation was used to convert from pixel values of MSB to grams via the expression

$$m_{pixel} = \frac{B_{obs}}{B_e} \times 1.97 \times 10^{-24} \text{ g} \quad (4.1)$$

where B_{obs} is the observed MSB of the pixel, B_e is the electron brightness calculated from the van de Hulst coefficients, and 1.97×10^{-24} g is a factor that converts the number of electrons to mass, assuming a completely ionized corona with a composition of 90% hydrogen and 10% helium. The known angle of propagation allowed the correct value of B_e to be computed resulting in a significant reduction in the uncertainties associated with the propagation angle. The largest remaining uncertainty is the unknown angular width along the LOS. This uncertainty was quantified in a similar approach to the method outlined in Vourlidas *et al.* (2000). This simulates the brightness of a CME with homogeneous density distribution and finite angular width along the LOS—longitudinal angular width $\Delta\theta_{long}$, al-

lowing calculation of a simulated observed mass. Comparing this to the actual mass allowed for an evaluation of CME mass underestimation for given values of $\Delta\theta_{long}$. Since the values for $\Delta\theta_{long}$ are unknown, the expression derived in Byrne *et al.* (2010) for the *latitudinal* angular width of this CME as a function of height, $\Delta\theta_{lat}(r) = 25r^{0.22}$, was used to define an upper limit to $\Delta\theta_{long}$. It was assumed the CME longitudinal angular width is no more than twice the latitudinal angular width, or $\Delta\theta_{long} \leq 2 \times \Delta\theta_{lat}$. Such an upper limit is in agreement with simulations of flux-rope CMEs which give a typical aspect ratio of broadside to axial angular extents of 1.6–1.9 (Krall & St. Cyr, 2006). Hence the value for $\Delta\theta_{long}$ at each height was used to obtain the simulated mass underestimation estimates described above. The heights and angular widths used in this study produced CME mass underestimation estimates of between 5–10% for finite angular width uncertainty. An extra mass uncertainty of 6% was added to account for the assumption of coronal abundance of 90% hydrogen and 10% helium which can lead to slight errors while converting from pixel values of MSB to grams (Vourlidas *et al.*, 2010).

To calculate the CME mass a user-selected area (the extent of the CME, for example) of the base difference image was chosen and the pixel values within this area were summed to obtain total mass. Figure 4.2 COR2 B images show an example of the sector over which pixels were summed (the smaller sectors indicate a different summing region used at a later stage). The selected area was chosen for each image in the time sequence of CME propagation so as to determine the mass variation with height in COR1 and 2 using both A and B. The selection of an area by a point and click method is of course a subjective identification of the the extent of the CME, so it is susceptible to user-generated uncertainties. To quantify these uncertainties the mass was obtained for each coronagraph image in the time sequence (as described above) and the process was repeated five times in order to obtain the mean CME mass for each image and the standard error on the mean. This standard error was defined as the uncertainty due to user bias in the point and click method of CME identification. The height at each measurement interval was taken to be the heliocentric distance of the CME apex in the image i.e., the apex of the front was chosen by simple point-and-click method. The uncertainty on the apex height was also found by the standard error on five runs.

The deflection of a small streamer during CME propagation produces negative pixels in the base difference images. The effect is particularly apparent in the COR1 images, Figure 4.1. It is difficult to unambiguously distinguish between streamer and CME, making it difficult to quantify the uncertainty introduced due to streamer interaction. To make an estimate of the streamer's effects, a calculation of its mass in the pre-event image was made. A number of different samples of the area of the streamer in the COR1B pre-event image that effects all subsequent images produced a mass estimate of $\sim 5 \times 10^{14}$ g. This mass was used as a measure of the uncertainty introduced due to streamer interaction in the COR1B images. A similar analysis of the COR1A pre-event images gave a streamer mass estimate of $\sim 7 \times 10^{14}$ g. COR2 images are relatively unaffected by significant changes in background coronal brightness and do not suffer from negative pixel values to as large an extent as COR1. The pre-event image of COR2B is particularly clean and free of background streamers, hence COR2B images are considered to provide most accurate CME mass estimation.

Finally, in order to obtain a more complete and continuous estimate of CME mass growth, the masses determined from both COR1 and COR2 coronagraphs were summed in those cases where image times of the inner and outer coronagraphs overlapped¹. The overlap in the inner and outer coronagraphs' fields of view was also taken into account in this summation.

A concise measurement of the CME kinematics, such as velocity and acceleration, were taken from the results of the study of Byrne *et al.* (2010). Since these kinematics take into account the true three dimensional surface of the front they provide reliable estimates of CME velocity and acceleration in 3-D space. These velocity and acceleration measurements were used in the calculation of kinetic energy and total force on the CME for each point in time. The CME mass used in all energy and force calculations was the asymptotic mass it approaches at later stages of its evolution beyond $10 R_{\odot}$ as observed from the *STEREO B* spacecraft i.e., $3.4 \pm 1.0 \times 10^{15}$ g. As will be shown, there is good motivation for the use of constant mass in the magnitude of kinetic energy and force estimates.

¹A difference in cadence of the inner and outer coronagraphs means that the images closest in time have a three minute offset e.g., a COR1 image taken at 07:25 UT was considered to be coincident in time with the COR2 image at 07:22 UT

4.1.3 Masses

The results of the calculation for CME mass development with time and height for both *STEREO* A and B coronagraphs are shown in Figure ???. In panel (a), the height values are those taken from a point-and-click method of tracking the CME apex; these heights are corrected for CME propagation angle of $\sim 45^\circ$. In both panels (a) and (b), the mass estimates of *STEREO* A and B follow a similar trend and have similar values at each stage in the propagation. Such good agreement between mass values is a good indicator that $\sim 45^\circ$ is the correct angle of propagation from the sky-plane. A change in the cadence of mass measurements is noticeable at $\sim 08:00$ UT (or $\gtrsim 5 R_\odot$). This is due to the use of only COR1 images (with a cadence of 10 minutes) prior to this time, and the use of the COR2 plus COR1 images after this time (the cadence of these measurements follows that of COR2 – 30 minutes). Comparing A and B below $4.5 R_\odot$, mass values show a similar trend and increase at the same rate, but at approximately $3 R_\odot$ the mass measurements in COR1 B appear to increase to a much larger value than fall again. This effect is visible in the COR1 A measurements, albeit diminished. It is probably due to the presence of a prominence which contains a significant mass content and therefore contributes a large amount to total measured CME mass. Also, early on in its propagation, the prominence may still be emitting H- α line radiation (656.28 nm) due to the larger fraction of neutral hydrogen at its cooler temperatures.

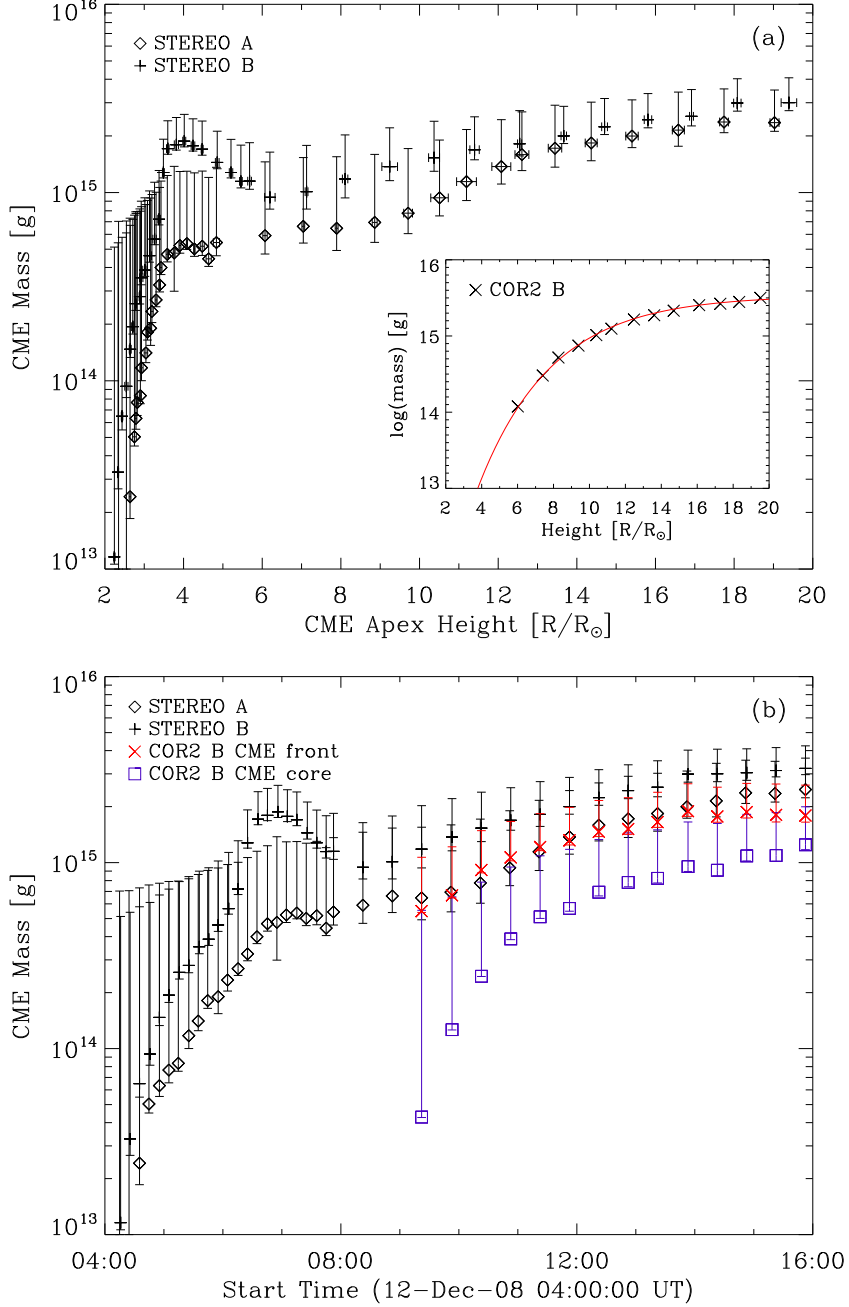


Figure 4.4: CME mass development with height (a) and time (b), for the 2008 December 12 CME. After $\sim 08:00$ UT ($\gtrsim 5 R_\odot$) the masses from the inner and outer coronagraphs are summed to show uninterrupted mass development from ~ 2 – $20 R_\odot$ over a period of 12 hours. The small bump in the CME mass at $\sim 07:00$ UT ($\sim 4 R_\odot$) is probably due to an unknown amount of H- α emission from the prominence. Mass of CME front and core are also shown, red ‘ \times ’ and blue square, for COR2 B, panel (b). After 14:52 UT they share approximately equal mass. The inset of (a) shows mass development with height for COR2 B only; the red curve represents a fit to the data whereby the mass asymptotically approaches $3.4 \pm 1.0 \times 10^{15}$ g.

The COR1 imaging passband is centered on H- α so any emission in the prominence from neutral hydrogen could be contributing to light received by the COR1 coronagraphs, this is apparent from the saturation region in the COR1 B images in Figure 4.1. Since this is resonance line emission, and not Thomson scattered emission, it leads to an erroneous measurement in CME mass. Thus, it is assumed the larger rise and fall in CME mass is caused by the prominence entering and exiting the COR1 B field of view. The effect is diminished in COR1 A since the prominence does not enter the FOV to as large an extent as in COR1 B. The interpretation that the ‘mass bump’ is not actual mass growth (or loss) is supported by previous measurements where CME mass increase follows a trend with height described by $M_{cme}(h) = M_a(1 - e^{-h/h_a})$, where M_a is the final mass the CME approaches asymptotically and h_a is the height at which the CME reaches $0.63M_a$ (Colaninno & Vourlidas, 2009), with no ‘bump’ in mass earlier on. The decline in mass after the peak may be explained by the ionization of neutral hydrogen such that H- α emission diminishes and simply becomes Thomson scattering of free electrons, as with the rest of the CME material.

In order to produce a fit to the data, the COR2 B mass results were chosen because its pre-event image was largely free of any bright streamers or other features which introduce unwanted effects in the production of base difference images, as described above. A fit with the above equation resulted in a final asymptotic CME mass of $3.4 \pm 1.0 \times 10^{15}$ g, with a scale height of $h_a = 2.9 R_\odot$. This fit is plotted along with the COR2 B data in the inset panel of Figure ??(a). Note that the mass increase is due to material coming up from below the occulting disk, and not actual mass gain of the CME. The uncertainty on the above asymptotic mass value was taken to be 30%, from the largest uncertainty due to finite width, the conversion factor uncertainty as described above, the standard error user-generated uncertainty, and uncertainty due to streamer interaction.

In each image where the CME core and front are distinguishable, their masses were measured separately. This was carried out by user selected regions demarcating the areas of core and front, see COR2 B at 12:22 UT and 14:52 UT in Figure 4.2 for an example of the separate core and front sectors over which pixel values were summed to obtain total mass. The uncertainties due to finite width of the observed object also apply to the core and front measurements, however,

since the widths of these particular areas of the CME are unknown we chose the maximum uncertainty of 10% from the above analysis since neither core nor front can be any wider than the maximum width assigned to this CME. The remaining uncertainties described above were also applied. The mass development of core and front with time is shown in Figure ??(b). The two mass measurements are subject to an observational effect of apparent exponential mass growth, however by the time the CME is fully in the field of view at 14:45 UT the core and front share approximately equal mass.

4.2 Energies and Dynamics

In the following calculations, all measurements of force and kinetic energy use the asymptotic mass of $3.4 \pm 1.0 \times 10^{15}$ g and not the instantaneous mass values calculated from each coronagraph image i.e., the CME is considered to begin its propagation with this mass and does not acquire any mass as it propagates.

Estimates of the force and kinetic energy use the 3-D velocity and acceleration measurements produced by Byrne *et al.* (2010). Their method firstly identifies the CME front in each coronagraph image using a multiscale edge detection filter. The front edges were then used to define a quadrilateral in space into which an ellipse is fit, this method is known as elliptical tie-pointing. This was done for multiple horizontal planes through the CME so that the fit ellipses outline a curved front in 3-D space. The speed and acceleration were then deduced from the change in position of the front, with time, through the *STEREO* COR1, COR2 and HI fields of view. Since mass measurements in this study use only the COR1 and COR2 coronagraphs, HI kinematics measurements have been excluded here. The CME front position uncertainty in *STEREO A* and *B* coronagraphs was determined from the filter width in the multiscale analysis. Velocity and acceleration uncertainties were then propagated from position uncertainty. Figure ??(a) shows CME velocity as a function of heliocentric distance, along with acceleration in panel (b).

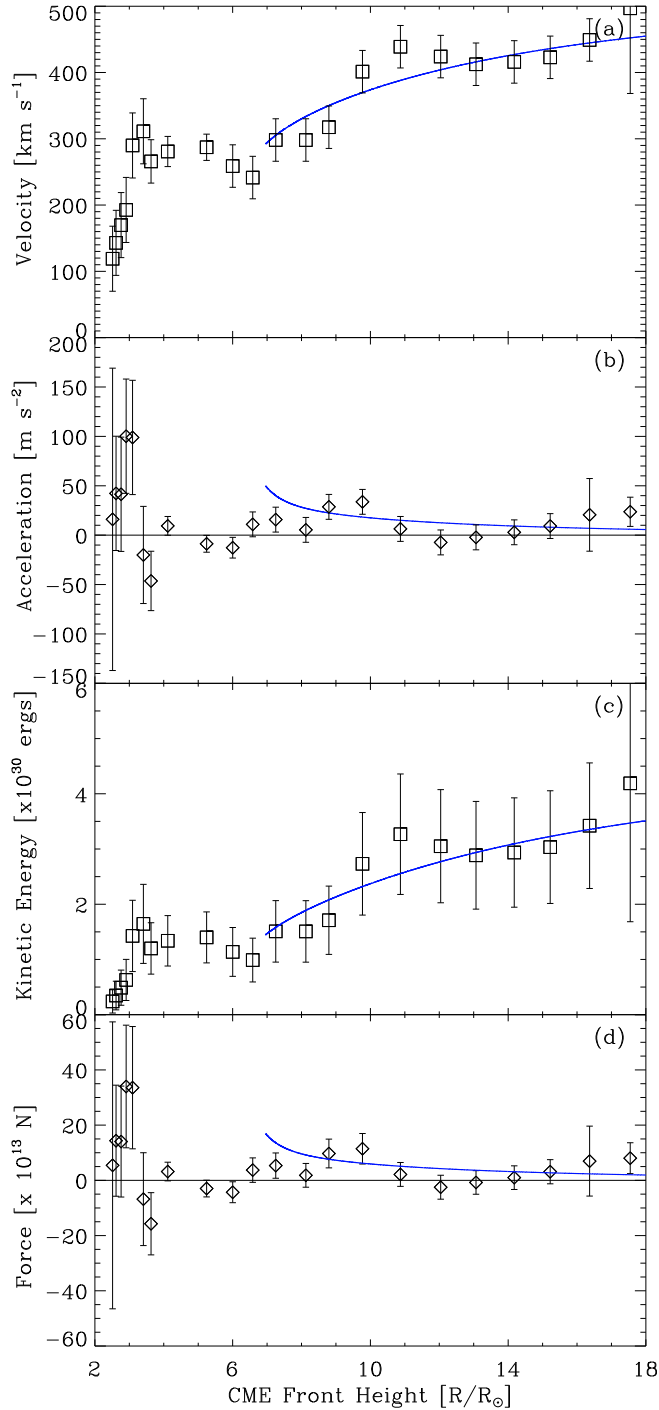


Figure 4.5: (a) CME velocity as a function of heliocentric distance, including a fit to the data produced using an aerodynamic drag model beyond $\sim 7 R_\odot$ (Byrne *et al.*, 2010). (b) Acceleration of CME, including fit, derived from the velocity data and fit. Panel (c) and (d) show the kinetic energy and force, respectively, both calculated using constant CME mass of $3.4 \pm 1.0 \times 10^{15} \text{ g}$ and kinematics results from (a) and (b). Also shown are the fits to energy and force produced from fits to velocity and acceleration.

4.2 Energies and Dynamics

The CME kinetic energy was calculated using $E_{kin} = 1/2M_{cme}v_{cme}^2$, where M_{cme} is the final asymptotic mass of $3.4 \pm 1.0 \times 10^{15}$ g and v_{cme} are the instantaneous velocity measurements, results of this calculation are shown in Figure ??(c). The kinetic energy shows an initial rise towards $6.3 \pm 3.7 \times 10^{29}$ ergs at $\sim 3 R_\odot$, beyond which it rises steadily to $4.2 \pm 2.5 \times 10^{30}$ ergs at $\sim 18 R_\odot$, these values are similar to those reported in Vourlidas *et al.* (2000, 2010) and Emslie *et al.* (2004).

The total force on the CME was calculated using $F_{total} = M_{cme}a_{cme}$, where M_{cme} is as above and a_{cme} is taken from the instantaneous acceleration values. As shown in panel (d) of Figure ??, the force initially grows significantly, reaching a maximum value of $3.4 \pm 2.2 \times 10^{14}$ N at $\sim 3 R_\odot$. The early rise and fall in acceleration (or force) is in agreement with a previous study of a CME observed to reach peak acceleration at $\sim 1.7 R_\odot$ after which it reaches a constant velocity beyond $\sim 3.4 R_\odot$ (Gallagher *et al.*, 2003). Such results are also found in a statistical study which shows that the majority of CMEs have peak acceleration in the low corona with a mean height of maximum acceleration at $1.5 R_\odot$ (Bein *et al.*, 2011). Similarly, observational studies by Zhang *et al.* (2001) and Zhang *et al.* (2004) also show early phase peak acceleration between $2\text{--}5 R_\odot$ and forces on the order of 10^{15} N and 10^{12} N, depending on whether the CME shows large initial acceleration or a slow, more gradual acceleration.

After this early peak, the force drops to an average value of $3.8 \pm 5.4 \times 10^{13}$ N at distances between $7\text{--}18 R_\odot$. It is apparent from Figure ??(a) that the velocity continues to increase beyond $7 R_\odot$, implying that a positive radial force must be present. To clarify this, a fit to the velocity data using a model for solar wind drag on the CME beyond $7 R_\odot$ (as outlined in Byrne *et al.* (2010)) is shown in Figure ??(a). Although the data suggest a non-monotonic increase in velocity, the fit reveals that propagation is best described by a steadily increasing velocity between $7\text{--}18 R_\odot$. The acceleration and kinetic energy curves derived from this velocity fit are shown in Figure ??(b) and (c). In Figure ??(d), the curve for the force derived from the velocity fit initially deviates from the data at $\sim 7 R_\odot$, however beyond this distance there is good agreement with the data and the derived force is entirely positive. This suggests that the solar wind exerts a positive aerodynamic drag force on the CME, resulting in a velocity that approaches the asymptotic solar wind speed at large heliospheric distances.

4.2.1 Forces acting on CMEs

It should be noted that Figure ?? shows an overall exponential increase in CME mass with height which could be interpreted as the CME rapidly gaining mass as it propagates. Care should be taken with this interpretation since this apparent exponential mass increase is almost certainly due to the CME moving into the field of view, therefore allowing us to measure more of its mass content; such an interpretation is in agreement with similar assertions made in Vourlidas *et al.* (2010). It is difficult to distinguish between actual CME mass growth and an apparent growth due to more of the CME being observed. If the initial early rise in CME mass is assumed to be an observational artifact then we can interpret the CME mass to be in the range of $(3\text{--}3.5)\times 10^{15}$ g for most of its early propagation i.e., the CME already has such a mass before launch and does not acquire more mass (via inflows or otherwise) during propagation. Such an interpretation is in agreement with CME mass measurements calculated from dimmings in *STEREO* Extreme Ultraviolet Image (EUVI) images, which show the mass calculated from EUV images to be approximately equal to CME mass in COR2 images, $m_{\text{EUVI}}/m_{\text{COR2}} = 1.1 \pm 0.3$ (Aschwanden *et al.*, 2009). Once the CME bubble is in the field of view at $\sim 10 R_\odot$ the mass in its entirety can be measured and the increase beyond this point, if any, is slow and steady, Figure ??.

The early stages of CME propagation are dominated by a sharp rise to a peak force of $3.4 \pm 2.2 \times 10^{14}$ N at $\sim 3 R_\odot$ followed by a sharp decline, Figure ??(d). The catastrophe model (Forbes & Isenberg, 1991; Forbes & Priest, 1995; Lin & Forbes, 2000), magnetic breakout model (Antiochos *et al.*, 1999b; Lynch *et al.*, 2008), and toroidal instability model (Chen, 1996; Kliem & Török, 2006) employ a number of forces acting on the CME to produce an over all acceleration into interplanetary space. For example, the toroidal instability model used by Chen (1996) uses a Lorentz hoop force (or Lorentz self-force), solar wind drag, and gravity to provide a net force acting on the CME between $2\text{--}3 R_\odot$ that quickly rises to a peak total force of $\sim 10^{16}$ N and then falls rapidly.

If we assume that the peak force observed for the 2008 December 12 CME is the net force due to similar forces used in the above models, such as the solar wind drag, gravity, and some form of magnetic CME driver e.g., a $\mathbf{J} \times \mathbf{B}$ force,

4.2 Energies and Dynamics

we may estimate their relative contribution. The force due to solar wind drag on the CME is given by

$$\mathbf{F}_d = -\frac{1}{2}C_d\rho_{sw}A_{cme}(\mathbf{v} - \mathbf{v}_{sw}) \mid \mathbf{v} - \mathbf{v}_{sw} \mid \quad (4.2)$$

where M_{cme} is the CME mass, \mathbf{v} is the CME velocity, C_d is the drag coefficient, ρ_{sw} is the solar wind mass density, A_{cme} is the CME area exposed to solar wind drag and \mathbf{v}_{sw} is the solar wind velocity (Maloney & Gallagher, 2010). To estimate the effects of this force we use $\rho_{sw} = n_p m_p$, where m_p is proton mass, and assume ionization fraction of $\chi = 1$ such that $n_p = n_e [cm^{-3}]$. Electron density, and hence proton density, is then given by an interplanetary density model derived from a special solution of the Parker solar wind equation (Mann *et al.*, 1999), solar wind velocity values as a function of height are also determined using this model. A_{cme} is estimated using the expression derived in Byrne *et al.* (2010) for latitudinal angular width of the CME as a function of height, $\Delta\theta_{lat}(r) = 26r^{0.22}$. This is used to derive an arc length of the CME front and, as above, making the assumption $\Delta\theta_{long} = 2 \times \Delta\theta_{lat}$, the two arc lengths derived from these angles then give the surface that the solar wind acts on, thus $A_{cme} = 1352r^{2.44}$. Setting the drag coefficient $C_d = 1$, and using the Mann *et al.* (1999) model to derive a density and a solar wind velocity of $2.3 \times 10^5 \text{ cm}^{-3}$ and 70 km s^{-1} , respectively, equation [1] then gives a force of $\mathbf{F}_d = -8.0 \times 10^{12} \hat{r} \text{ N}$ for solar wind drag at $\sim 3 R_\odot$, where \hat{r} is a unit vector in the positive radial direction.

A simple estimate of force due to gravity is given by $\mathbf{F}_g = GM_\odot M_{cme}/\mathbf{r}^2$, where G is the universal gravitational constant, M_\odot is solar mass, M_{cme} is CME mass, and \mathbf{r} is a heliocentric position vector¹. Given a CME mass of $3.4 \times 10^{15} \text{ g}$ the force due to gravity at a heliocentric distance of $3 R_\odot$ is $\mathbf{F}_g = -1.0 \times 10^{14} \hat{r} \text{ N}$. The only remaining contribution is due to some form of magnetic CME driver, F_{mag} , which is estimated using

$$\mathbf{F}_{mag} = \mathbf{F}_{total} - \mathbf{F}_d - \mathbf{F}_g \quad (4.3)$$

¹Ideally the heliocentric distance of the CME centre of mass would be used here. However an unknown amount of mass is obscured by the coronagraphs occulting disk, making the mass distribution and hence COM difficult to determine. Thus the CME front height is used in the calculation of force due to gravity

(the pressure gradient in the CME equation of motion is assumed to be negligible and has been omitted here). Using the above values, the total magnetic contribution to CME force is calculated to be $\mathbf{F}_{mag} \approx 4.5 \times 10^{14} \hat{r} \text{ N}$ at $3 R_\odot$, indicating that this is the largest driver of CMEs at low coronal heights. Lorentz force dominated dynamics in early phase CME propagation are reported in Bein *et al.* (2011), in which a statistical study of a large sample of CMEs in EUVI, COR1, and COR2 indicated an early phase acceleration for the majority of CMEs that is attributable to a Lorentz force. A similar result of an observational study by Vršnak (2006) found that the Lorentz force plays a dominant role within a few solar radii. It should be noted that although we have labelled the force F_{mag} , there is no distinction on the exact form of this force e.g., whether it is magnetic pressure, magnetic tension, or a Lorentz self-force that acts as the driver. Also, any non-radial motion of the CME, such as that described in Byrne *et al.* (2010), is not taken into account here; any force estimates are purely radial in direction.

4.3 Conclusion

The *STEREO* COR1/2 coronagraphs have been used to determine the mass development of the 2008 December 12 CME. Knowledge of the longitudinal propagation angle of the CME allowed for a significant reduction in the mass uncertainty, giving a final estimate of $3.4 \pm 1.0 \times 10^{15} \text{ g}$. Using kinematics results of a previous study (Byrne *et al.*, 2010), the velocity and acceleration of the CME were combined with the mass measurements to determine the kinetic energy and total force on the CME. The early phase propagation of the CME was found to be dominated by a force of peak magnitude of $3.4 \pm 2.2 \times 10^{14} \text{ N}$ at $\sim 3.0 R_\odot$, after which the magnitude declines rapidly and settles to an average of $3.8 \pm 5.4 \times 10^{13} \text{ N}$. This early rise and fall in total force (or acceleration) is in agreement with previous observations of CME kinematics (Bein *et al.*, 2011; Gallagher *et al.*, 2003). Similarly, results of observational studies by Zhang *et al.* (2001) and Zhang *et al.* (2004) also show early phase peak acceleration between $2\text{--}5 R_\odot$ and forces on the order of 10^{15} N and 10^{12} N . The kinetic energy shows an initial rise towards $6.3 \pm 3.7 \times 10^{29} \text{ ergs}$ at $\sim 3 R_\odot$, beyond which it rises steadily to $4.2 \pm 2.5 \times 10^{30} \text{ ergs}$ at $\sim 18 R_\odot$, such order of magnitudes are similar to those reported in Emslie *et al.*

4.3 Conclusion

(2004); Vourlidas *et al.* (2000) and are typical of CME kinetic energies (Vourlidas *et al.*, 2010).

Such CME kinematics and dynamics property estimates cannot be carried out when unknown propagation angle hinders an accurate calculation of CME mass, hence adding unacceptable uncertainty to any subsequent calculations. This highlights the need for similar studies using the *STEREO* mission's ability to accurately determine the physical properties of CMEs, such as mass, with remarkably reduced uncertainty. Increasing the accuracy of force estimates of other well studied CMEs will allow for a more complete view of the magnitude of the forces influencing CME propagation and will allow model parameters to be more accurately constrained.

5

Coronal Mass Ejection Masses, Shocks, and Particle Acceleration

5.1 Radio Bursts

5.1.1 Type II, Type III, and Herringbones

5.2 EUV Wave and Radio Source

5.2.1 Relationship with Radio Spectra

5.3 Role of the CME

5.3.1 CME Bow Shock

5.3.2 Relationship Between CME, CBF, and Radio bursts

A

A Nice Appendix

This is where the appendix would go...

References

- ALY, J.J. (1991). How much energy can be stored in a three-dimensional force-free magnetic field? *Astrophysical Journal Letters*, **375**, L61–L64. (Cited on page 27.)
- ANTIOCHOS, S.K., DEVORE, C.R. & KLIMCHUK, J.A. (1999a). A Model for Solar Coronal Mass Ejections. *Astrophysical Journal*, **510**, 485–493. (Cited on page 27.)
- ANTIOCHOS, S.K., DEVORE, C.R. & KLIMCHUK, J.A. (1999b). A Model for Solar Coronal Mass Ejections. *Astrophysical Journal*, **510**, 485–493. (Cited on pages 43 and 58.)
- ASCHWANDEN, M.J., NITTA, N.V., WUELSER, J.P., LEMEN, J.R., SANDMAN, A., VOURLIDAS, A. & COLANINNO, R.C. (2009). First Measurements of the Mass of Coronal Mass Ejections from the EUV Dimming Observed with STEREO EUVI A+B Spacecraft. *Astrophysical Journal*, **706**, 376–392. (Cited on page 58.)
- AULANIER, G., DELUCA, E.E., ANTIOCHOS, S.K., McMULLEN, R.A. & GOLUB, L. (2000). The Topology and Evolution of the Bastille Day Flare. *Astrophysical Journal*, **540**, 1126–1142. (Cited on page 29.)
- BABCOCK, H.W. (1961). The Topology of the Sun’s Magnetic Field and the 22-YEAR Cycle. *Astrophysical Journal*, **133**, 572. (Cited on page 10.)
- BEIN, B.M., BERKEBILE-STOISER, S., VERONIG, A.M., TEMMER, M., MUHR, N., KIENREICH, I., UTZ, D. & VRŠNAK, B. (2011). Impulsive Acceleration of Coronal Mass Ejections. I. Statistics and Coronal Mass Ejection Source Region Characteristics. *Astrophysical Journal*, **738**, 191–+. (Cited on pages 57 and 60.)
- BILLINGS, D.E. (1966). *A guide to the solar corona*. (Cited on pages 44 and 48.)
- BONG, S.C., MOON, Y.J., CHO, K.S., KIM, Y.H., PARK, Y.D. & CHOE, G.S. (2006). Direct Observation of Low Coronal Breakout: Does Breakout Precede or Follow Solar Eruption? *Astrophysical Journal Letters*, **636**, L169–L172. (Cited on page 29.)
- BRUECKNER, G.E., HOWARD, R.A., KOOMEN, M.J., KORENDYKE, C.M., MICHELS, D.J., MOSES, J.D., SOCKER, D.G., DERE, K.P., LAMY, P.L., LLEBARIA, A., BOUT, M.V., SCHWENN, R., SIMNETT, G.M., BEDFORD, D.K. & EYLES, C.J. (1995). The Large Angle Spectroscopic Coronagraph (LASCO). *Solar Physics*, **162**, 357–402. (Cited on page 44.)
- BYRNE, J.P., MALONEY, S.A., MCATEER, R.T.J., REFOJO, J.M. & GALLAGHER, P.T. (2010). Propagation of an Earth-directed coronal mass ejection in three dimensions. *Nature Communications*, **1**. (Cited on pages xv, 44, 49, 50, 51, 55, 56, 57, 59 and 60.)

REFERENCES

- CARLSSON, M. & STEIN, R.F. (1997). Formation of Solar Calcium H and K Bright Grains. *Astrophysical Journal*, **481**, 500. (Cited on page 15.)
- CHARBONNEAU, P. (2010). Dynamo Models of the Solar Cycle. *Living Reviews in Solar Physics*, **7**, 3. (Cited on page 11.)
- CHEN, J. (1989). Effects of toroidal forces in current loops embedded in a background plasma. *Astrophysical Journal*, **338**, 453–470. (Cited on pages xiii, 29 and 31.)
- CHEN, J. (1996). Theory of prominence eruption and propagation: Interplanetary consequences. *Journal of Geophysical Research*, **1012**, 27499–27520. (Cited on pages 44 and 58.)
- CHEN, J., MARQUÉ, C., VOURLIDAS, A., KRALL, J. & SCHUCK, P.W. (2006). The Flux-Rope Scaling of the Acceleration of Coronal Mass Ejections and Eruptive Prominences. *Astrophysical Journal*, **649**, 452–463. (Cited on page 44.)
- COLANINNO, R.C. & VOURLIDAS, A. (2009). First Determination of the True Mass of Coronal Mass Ejections: A Novel Approach to Using the Two STEREO Viewpoints. *Astrophysical Journal*, **698**, 852–858. (Cited on pages 45 and 54.)
- DAVIS, R., HARMER, D.S. & HOFFMAN, K.C. (1968). Search for Neutrinos from the Sun. *Physical Review Letters*, **20**, 1205–1209. (Cited on page 4.)
- DOMINGO, V., FLECK, B. & POLAND, A.I. (1995). The SOHO Mission: an Overview. *Solar Physics*, **162**, 1–37. (Cited on page 44.)
- EMSLIE, A.G., KUCHAREK, H., DENNIS, B.R., GOPALSWAMY, N., HOLMAN, G.D., SHARE, G.H., VOURLIDAS, A., FORBES, T.G., GALLAGHER, P.T., MASON, G.M., METCALF, T.R., MEWALDT, R.A., MURPHY, R.J., SCHWARTZ, R.A. & ZURBUCHEN, T.H. (2004). Energy partition in two solar flare/CME events. *Journal of Geophysical Research (Space Physics)*, **109**, A10104. (Cited on pages 57 and 60.)
- FAN, Y. (2009). Magnetic Fields in the Solar Convection Zone. *Living Reviews in Solar Physics*, **6**, 4. (Cited on page 11.)
- FELDMAN, U. & WIDING, K.G. (2003). Elemental Abundances in the Solar Upper Atmosphere Derived by Spectroscopic Means. *Space Science Reviews*, **107**, 665–720. (Not cited.)
- FITZPATRICK, R. (2000). *The Physics of Plasmas*. (Cited on pages xii and 21.)
- FONTENLA, J., REICHMANN, E.J. & TANDBERG-HANSSEN, E. (1988). The Lyman-alpha line in various solar features. I - Observations. *Astrophysical Journal*, **329**, 464–481. (Cited on pages xii, 13, 14 and 15.)
- FORBES, T.G. & ISENBERG, P.A. (1991). A catastrophe mechanism for coronal mass ejections. *Astrophysical Journal*, **373**, 294–307. (Cited on pages 43 and 58.)
- FORBES, T.G. & PRIEST, E.R. (1995). Photospheric Magnetic Field Evolution and Eruptive Flares. *Astrophysical Journal*, **446**, 377–+. (Cited on pages 43 and 58.)
- FOUKAL, P.V. (2004). *Solar Astrophysics, 2nd, Revised Edition*. Wiley-VCH. (Cited on page 2.)

REFERENCES

- FUKUDA, Y., HAYAKAWA, T., ICHIHARA, E., INOUE, K., ISHIHARA, K., ISHINO, H., ITOW, Y., KAJITA, T., KAMEDA, J., KASUGA, S., KOBAYASHI, K., KOBAYASHI, Y., KOSHIO, Y., MARTENS, K., MIURA, M., NAKAHATA, M., NAKAYAMA, S., OKADA, A., OKETA, M., OKUMURA, K., OTA, M., SAKURAI, N., SHIOZAWA, M., SUZUKI, Y., TAKEUCHI, Y., TOTSUKA, Y., YAMADA, S., EARL, M., HABIG, A., HONG, J.T., KEARNS, E., KIM, S.B., MASUZAWA, M., MESSIER, M.D., SCHOLBERG, K., STONE, J.L., SULAK, L.R., WALTER, C.W., GOLDHABER, M., BARSZCZAK, T., GAJEWSKI, W., HALVERSON, P.G., HSU, J., KROPP, W.R., PRICE, L.R., REINES, F., SOBEL, H.W., VAGINS, M.R., GANEZER, K.S., KEIG, W.E., ELLSWORTH, R.W., TASAKA, S., FLANAGAN, J.W., KIBAYASHI, A., LEARNED, J.G., MATSUNO, S., STENGER, V., TAKEMORI, D., ISHII, T., KANZAKI, J., KOBAYASHI, T., NAKAMURA, K., NISHIKAWA, K., OYAMA, Y., SAKAI, A., SAKUDA, M., SASAKI, O., ECHIGO, S., KOHAMA, M., SUZUKI, A.T., HAINES, T.J., BLAUFUSS, E., SANFORD, R., SVOBODA, R., CHEN, M.L., CONNER, Z., GOODMAN, J.A., SULLIVAN, G.W., MORI, M., HILL, J., JUNG, C.K., MAUGER, C., McGREW, C., SHARKEY, E., VIREN, B., YANAGISAWA, C., DOKI, W., ISHIZUKA, T., KITAGUCHI, Y., KOGA, H., MIYANO, K., OKAZAWA, H., SAJI, C., TAKAHATA, M., KUSANO, A., NAGASHIMA, Y., TAKITA, M., YAMAGUCHI, T., YOSHIDA, M., ETOH, M., FUJITA, K., HASEGAWA, A., HASEGAWA, T., HATAKEYAMA, S., IWAMOTO, T., KINEBUCHI, T., KOGA, M., MARUYAMA, T., OGAWA, H., SUZUKI, A., TSUSHIMA, F., KOSHIBA, M., NEMOTO, M., NISHIJIMA, K., FUTAGAMI, T., HAYATO, Y., KANAYA, Y., KANEYUKI, K., WATANABE, Y., KIELCZEWSKA, D., DOYLE, R., GEORGE, J., STACHYRA, A., WAI, L., WILKES, J. & YOUNG, K. (1998). Measurements of the Solar Neutrino Flux from Super-Kamiokande's First 300 Days. *Physical Review Letters*, **81**, 1158–1162. (Cited on page 4.)
- GABRIEL, A.H. (1976). A magnetic model of the solar transition region. *Royal Society of London Philosophical Transactions Series A*, **281**, 339–352. (Cited on pages xii, 13, 14 and 15.)
- GALLAGHER, P.T., LAWRENCE, G.R. & DENNIS, B.R. (2003). Rapid Acceleration of a Coronal Mass Ejection in the Low Corona and Implications for Propagation. *Astrophysical Journal Letters*, **588**, L53–L56. (Cited on pages 57 and 60.)
- GEISS, J. (1985). Diagnostics of corona by in-situ composition measurements at 1 AU. In E. Rolfe & B. Battinck, eds., *Future Missions in Solar, Heliospheric & Space Plasma Physics*, vol. 235 of *ESA Special Publication*, 37–50. (Not cited.)
- HOWARD, R.A., MOSES, J.D., VOURLIDAS, A., NEWMARK, J.S., SOCKER, D.G., PLUNKETT, S.P., KORENDYKE, C.M., COOK, J.W., HURLEY, A., DAVILA, J.M., THOMPSON, W.T., ST CYR, O.C., MENTZELL, E., MEHALICK, K., LEMEN, J.R., WUELTER, J.P., DUNCAN, D.W., TARBELL, T.D., WOLFSON, C.J., MOORE, A., HARRISON, R.A., WALTHAM, N.R., LANG, J., DAVIS, C.J., EYLES, C.J., MAPSON-MENARD, H., SIMNETT, G.M., HALAIN, J.P., DEFISE, J.M., MAZY, E., ROCHUS, P., MERCIER, R., RAVET, M.F., DELMOTTE, F., AUCHERE, F., DELABOUDINIÈRE, J.P., BOTHMER, V., DEUTSCH, W., WANG, D., RICH, N., COOPER, S., STEPHENS, V., MAAHS, G., BAUGH, R., McMULLIN, D. & CARTER, T. (2008). Sun Earth Connection Coronal and Heliospheric Investigation (SECCHI). *Space Science Reviews*, **136**, 67–115. (Cited on pages xiv, 39, 42 and 44.)
- HOWARD, T.A. & TAPPIN, S.J. (2009a). Interplanetary Coronal Mass Ejections Observed in the Heliosphere: 1. Review of Theory. *Space Science Reviews*, **147**, 31–54. (Cited on page 37.)

REFERENCES

- HOWARD, T.A. & TAPPIN, S.J. (2009b). Interplanetary Coronal Mass Ejections Observed in the Heliosphere: 1. Review of Theory. *Space Science Reviews*, **147**, 31–54. (Cited on page 48.)
- HOWARD, T.A., FRY, C.D., JOHNSTON, J.C. & WEBB, D.F. (2007). On the Evolution of Coronal Mass Ejections in the Interplanetary Medium. *Astrophysical Journal*, **667**, 610–625. (Cited on page 44.)
- KABIN, K. (2001). A note on the compression ratio in MHD shocks. *Journal of Plasma Physics*, **66**, 259–274. (Cited on page 24.)
- KAISER, M.L., KUCERA, T.A., DAVILA, J.M., ST. CYR, O.C., GUHATHAKURTA, M. & CHRISTIAN, E. (2008). The STEREO Mission: An Introduction. *Space Science Reviews*, **136**, 5–16. (Cited on pages 38 and 44.)
- KLIEM, B. & TÖRÖK, T. (2006). Torus Instability. *Physical Review Letters*, **96**, 255002–+. (Cited on pages 44 and 58.)
- KRALL, J. & ST. CYR, O.C. (2006). Flux-Rope Coronal Mass Ejection Geometry and Its Relation to Observed Morphology. *Astrophysical Journal*, **652**, 1740–1746. (Cited on page 50.)
- KRALL, J., CHEN, J., DUFFIN, R.T., HOWARD, R.A. & THOMPSON, B.J. (2001). Erupting Solar Magnetic Flux Ropes: Theory and Observation. *Astrophysical Journal*, **562**, 1045–1057. (Cited on pages 30 and 31.)
- LIN, C.H., GALLAGHER, P.T. & RAFTERY, C.L. (2010). Investigating the driving mechanisms of coronal mass ejections. *Astronomy & Astrophysics*, **516**, A44. (Cited on page 44.)
- LIN, J. & FORBES, T.G. (2000). Effects of reconnection on the coronal mass ejection process. *Journal of Geophysical Research*, **105**, 2375–2392. (Cited on pages 43 and 58.)
- LYNCH, B.J., ANTIOCHOS, S.K., MACNEICE, P.J., ZURBUCHEN, T.H. & FISK, L.A. (2004). Observable Properties of the Breakout Model for Coronal Mass Ejections. *Astrophysical Journal*, **617**, 589–599. (Cited on pages 27 and 29.)
- LYNCH, B.J., ANTIOCHOS, S.K., DEVORE, C.R., LUHMANN, J.G. & ZURBUCHEN, T.H. (2008). Topological Evolution of a Fast Magnetic Breakout CME in Three Dimensions. *Astrophysical Journal*, **683**, 1192–1206. (Cited on pages xiii, 28, 44 and 58.)
- LYOT, B. (1939). The study of the solar corona and prominences without eclipses (George Darwin Lecture, 1939). *Monthly Notices of the Royal Astronomical Society*, **99**, 580. (Cited on page 38.)
- MACNEICE, P., ANTIOCHOS, S.K., PHILLIPS, A., SPICER, D.S., DEVORE, C.R. & OLSON, K. (2004). A Numerical Study of the Breakout Model for Coronal Mass Ejection Initiation. *Astrophysical Journal*, **614**, 1028–1041. (Cited on page 29.)
- MALONEY, S.A. & GALLAGHER, P.T. (2010). Solar Wind Drag and the Kinematics of Interplanetary Coronal Mass Ejections. *Astrophysical Journal Letters*, **724**, L127–L132. (Cited on pages 44 and 59.)

REFERENCES

- MANN, G., JANSEN, F., MACDOWALL, R.J., KAISER, M.L. & STONE, R.G. (1999). A heliospheric density model and type III radio bursts. *Astronomy & Astrophysics*, **348**, 614–620. (Cited on page 59.)
- MANOHARAN, P.K. & KUNDU, M.R. (2003a). Coronal Structure of a Flaring Region and Associated Coronal Mass Ejection. *Astrophysical Journal*, **592**, 597–606. (Cited on page 29.)
- MANOHARAN, P.K. & KUNDU, M.R. (2003b). Coronal Structure of a Flaring Region and Associated Coronal Mass Ejection. *Astrophysical Journal*, **592**, 597–606. (Cited on page 44.)
- MCATEER, R.T.J., GALLAGHER, P.T., WILLIAMS, D.R., MATHIOUDAKIS, M., PHILLIPS, K.J.H. & KEENAN, F.P. (2002). Long-Period Chromospheric Oscillations in Network Bright Points. *Astrophysical Journal Letters*, **567**, L165–L168. (Cited on page 15.)
- MELROSE, D.B. (1986). *Instabilities in Space and Laboratory Plasmas*. Cambridge University Press. (Cited on page 33.)
- MIKHEEV, S.P. & SMIRNOV, A.I. (1986). Resonant amplification of neutrino oscillations in matter and solar-neutrino spectroscopy. *Nuovo Cimento C Geophysics Space Physics C*, **9**, 17–26. (Cited on page 4.)
- MINNAERT, M. (1930). On the continuous spectrum of the corona and its polarisation. With 3 figures. (Received July 30, 1930). *Zeitschrift fur Astrophysik*, **1**, 209–+. (Cited on pages 44 and 48.)
- MITALAS, R. & SILLS, K.R. (1992). On the photon diffusion time scale for the sun. *Astrophysical Journal*, **401**, 759. (Cited on page 5.)
- MUNRO, R.H., GOSLING, J.T., HILDNER, E., MACQUEEN, R.M., POLAND, A.I. & ROSS, C.L. (1979). The association of coronal mass ejection transients with other forms of solar activity. *Solar Physics*, **61**, 201–215. (Cited on page 44.)
- PHILLIPS, K.J.H., FELDMAN, U. & LANDI, E. (2008). *Ultraviolet and X-ray Spectroscopy of the Solar Atmosphere*. Cambridge University Press. (Cited on pages xii, 13 and 14.)
- POLAND, A.I., HOWARD, R.A., KOOMEN, M.J., MICHELS, D.J. & SHEELEY, N.R., JR. (1981). Coronal transients near sunspot maximum. *Solar Physics*, **69**, 169–175. (Cited on page 44.)
- PRIEST, E. & FORBES, T. (2000). *Magnetic Reconnection*. (Cited on page 23.)
- ROBINSON, P.A., CAIRNS, I.H. & WILLES, A.J. (1994). Dynamics and efficiency of type III solar radio emission. *Astrophysical Journal*, **422**, 870–882. (Cited on page 33.)
- SCHRIJVER, C.J., ELMORE, C., KLIEM, B., TÖRÖK, T. & TITLE, A.M. (2008a). Observations and Modeling of the Early Acceleration Phase of Erupting Filaments Involved in Coronal Mass Ejections. *Astrophysical Journal*, **674**, 586–595. (Cited on page 31.)
- SCHRIJVER, C.J., ELMORE, C., KLIEM, B., TÖRÖK, T. & TITLE, A.M. (2008b). Observations and Modeling of the Early Acceleration Phase of Erupting Filaments Involved in Coronal Mass Ejections. *Astrophysical Journal*, **674**, 586–595. (Cited on page 44.)

REFERENCES

- STURROCK, P.A. (1991). Maximum energy of semi-infinite magnetic field configurations. *Astrophysical Journal*, **380**, 655–659. (Cited on page 27.)
- THOMPSON, M.J., CHRISTENSEN-DALSGAARD, J., MIESCH, M.S. & TOOMRE, J. (2003). The Internal Rotation of the Sun. *Annual Review of Astronomy & Astrophysics*, **41**, 599–643. (Cited on pages xi, 7 and 8.)
- THOMPSON, W.T. & REGINALD, N.L. (2008). The Radiometric and Pointing Calibration of SECCHI COR1 on STEREO. *Solar Physics*, **250**, 443–454. (Cited on pages xiii, 39 and 41.)
- TURCK-CHIÈZE, S. & COUVIDAT, S. (2011). Solar neutrinos, helioseismology and the solar internal dynamics. *Reports on Progress in Physics*, **74**, 086901. (Cited on pages 4, 5 and 7.)
- VAN DE HULST, H.C. (1950). The electron density of the solar corona. *Bulletin of the Astronomical Institutes of the Netherlands*, **11**, 135. (Cited on pages 44 and 48.)
- VERNAZZA, J.E., AVRETT, E.H. & LOESER, R. (1981). Structure of the solar chromosphere. III - Models of the EUV brightness components of the quiet-sun. *Astrophysical Journal Supplemental Series*, **45**, 635–725. (Cited on pages xii, 13, 14 and 15.)
- VOURLIDAS, A., SUBRAMANIAN, P., DERE, K.P. & HOWARD, R.A. (2000). Large-Angle Spectrometric Coronagraph Measurements of the Energetics of Coronal Mass Ejections. *Astrophysical Journal*, **534**, 456–467. (Cited on pages 45, 49, 57 and 61.)
- VOURLIDAS, A., BUZASI, D., HOWARD, R.A. & ESFANDIARI, E. (2002). Mass and energy properties of LASCO CMEs. In A. Wilson, ed., *Solar Variability: From Core to Outer Frontiers*, vol. 506 of *ESA Special Publication*, 91–94. (Cited on page 44.)
- VOURLIDAS, A., HOWARD, R.A., ESFANDIARI, E., PATSOURAKOS, S., YASHIRO, S. & MICHALEK, G. (2010). Comprehensive Analysis of Coronal Mass Ejection Mass and Energy Properties Over a Full Solar Cycle. *Astrophysical Journal*, **722**, 1522–1538. (Cited on pages 44, 50, 57, 58 and 61.)
- VRŠNAK, B. (2006). Forces governing coronal mass ejections. *Advances in Space Research*, **38**, 431–440. (Cited on page 60.)
- VRŠNAK, B. & GOPALSWAMY, N. (2002). Influence of the aerodynamic drag on the motion of interplanetary ejecta. *Journal of Geophysical Research (Space Physics)*, **107**, 1019. (Cited on page 24.)
- VRŠNAK, B., MAGDALENIĆ, J. & ZLOBEC, P. (2004). Band-splitting of coronal and interplanetary type II bursts. III. Physical conditions in the upper corona and interplanetary space. *Astronomy and Astrophysics*, **413**, 753–763. (Cited on page 25.)
- WOLFENSTEIN, L. (1978). Neutrino oscillations in matter. *Physical Review Letters*, **37**, 2369–2374. (Cited on page 4.)
- ZHANG, J., DERE, K.P., HOWARD, R.A., KUNDU, M.R. & WHITE, S.M. (2001). On the Temporal Relationship between Coronal Mass Ejections and Flares. *Astrophysical Journal*, **559**, 452–462. (Cited on pages 57 and 60.)

REFERENCES

- ZHANG, J., DERE, K.P., HOWARD, R.A. & VOURLIDAS, A. (2004). A Study of the Kinematic Evolution of Coronal Mass Ejections. *Astrophysical Journal*, **604**, 420–432. (Cited on pages 57 and 60.)